HHS Public Access

Author manuscript

ACS Appl Mater Interfaces. Author manuscript; available in PMC 2022 September 03.

Published in final edited form as:

ACS Appl Mater Interfaces. 2021 May 26; 13(20): 23423–23437. doi:10.1021/acsami.1c03415.

In Vivo Imaging of Allografted Glial-Restricted Progenitor Cell Survival and Hydrogel Scaffold Biodegradation

Shreyas Kuddannaya,

The Russell H. Morgan Department of Radiology and Radiological Science, Division of MR Research, The Johns Hopkins School of Medicine, Baltimore, Maryland 21205, United States; Cellular Imaging Section and Vascular Biology Program, Institute for Cell Engineering, The Johns Hopkins School of Medicine, Baltimore, Maryland 21205, United States

Wei Zhu,

The Russell H. Morgan Department of Radiology and Radiological Science, Division of MR Research, The Johns Hopkins School of Medicine, Baltimore, Maryland 21205, United States; Cellular Imaging Section and Vascular Biology Program, Institute for Cell Engineering, The Johns Hopkins School of Medicine, Baltimore, Maryland 21205, United States

Chengyan Chu,

The Russell H. Morgan Department of Radiology and Radiological Science, Division of MR Research, The Johns Hopkins School of Medicine, Baltimore, Maryland 21205, United States; Cellular Imaging Section and Vascular Biology Program, Institute for Cell Engineering, The Johns Hopkins School of Medicine, Baltimore, Maryland 21205, United States

Anirudha Singh,

Department of Urology, the James Buchanan Brady Urological Institute, The Johns Hopkins School of Medicine, Baltimore, Maryland 21287, United States; Department of Chemical & Biomolecular Engineering, The Johns Hopkins School of Medicine, Baltimore, Maryland 21205, United States

Corresponding Author: **Jeff W. M. Bulte** – The Russell H. Morgan Department of Radiology and Radiological Science, Division of MR Research, The Johns Hopkins School of Medicine, Baltimore, Maryland 21205, United States; Cellular Imaging Section and Vascular Biology Program, Institute for Cell Engineering and Department of Chemical & Biomolecular Engineering, The Johns Hopkins School of Medicine, Baltimore, Maryland 21205, United States; Department of Biomedical Engineering and Department of Oncology, The Johns Hopkins University School of Medicine, Baltimore, Maryland 21205, United States; jwmbulte@mri.jhu.edu.

Author Contributions

The manuscript was written through contributions of all authors. S.K. performed data curation, formal analysis, methodology, investigation, validation, and writing the original draft. W.Z. performed data curation, investigation, and validation. C.C. performed the investigation and methodology. A.S. did the conceptualization, formal analysis, methodology, and validation. P.W. did the methodology and validation. J.W.M.B. participated in the conceptualization, funding acquisition, methodology, project administration, resources, supervision, writing-review, and editing.

Complete contact information is available at: https://pubs.acs.org/10.1021/acsami.1c03415

Supporting Information

The Supporting Information is available free of charge at https://pubs.acs.org/doi/10.1021/acsami.1c03415.

Composite make-up of hydrogel formulations; hydrogel mesh sizes calculated from swelling data; antibodies used for immunohistological characterization; FTIR spectra of hydrogel precursors and the cross-linked hydrogel and SEM micrographs of cross-linked hydrogels; morphology of scaffolded mGRPs in 10 mg/mL composite gels at day 14; calibration curve of absorbance versus mGRP cell number for the CCK-8 proliferation assay; immunophenotyping of GFP^+ mGRPs and quantification of cells expressing phenotypic markers; immunohistochemistry of mGRP spheres; S.C transplanted mGRP survival; and Iba-1 immunohistological staining and autofluorescence assessment (PDF)

The authors declare no competing financial interest.

Piotr Walczak,
Center for Advanced Imaging Research, Department of Diagnostic Radiology and Nuclear Medicine, University of Maryland, Baltimore, Maryland 21201, United States

Jeff W. M. Bulte
The Russell H. Morgan Department of Radiology and Radiological Science, Division of MR Research, The Johns Hopkins School of Medicine, Baltimore, Maryland 21205, United States; Cellular Imaging Section and Vascular Biology Program, Institute for Cell Engineering and Department of Chemical & Biomolecular Engineering, The Johns Hopkins School of Medicine, Baltimore, Maryland 21205, United States; Department of Biomedical Engineering and Department of Oncology, The Johns Hopkins University School of Medicine, Baltimore, Maryland 21205, United States

Abstract

Transplanted glial-restricted progenitor (GRP) cells have potential to focally replace defunct astrocytes and produce remyelinating oligodendrocytes to avert neuronal death and dysfunction. However, most central nervous system cell therapeutic paradigms are hampered by high initial cell death and a host antigraft immune response. We show here that composite hyaluronic acid-based hydrogels of tunable mechanical strengths can significantly improve transplanted GRP survival and differentiation. Allogeneic GRPs expressing green fluorescent protein and firefly luciferase were scaffolded in optimized hydrogel formulations and transplanted intracerebrally into immunocompetent BALB/c mice followed by serial *in vivo* bioluminescent imaging and chemical exchange saturation transfer magnetic resonance imaging (CEST MRI). We demonstrate that gelatin-sensitive CEST MRI can be exploited to monitor hydrogel scaffold degradation *in vivo* for ~5 weeks post transplantation without necessitating exogenous labeling. Hydrogel scaffolding of GRPs resulted in a 4.5-fold increase in transplanted cell survival at day 32 post transplantation compared to naked cells. Histological analysis showed significant enhancement of cell proliferation as well as $Olig2^+$ and $GFAP^+$ cell differentiation for scaffolded cells compared to naked cells, with reduced host immunoreactivity. Hence, hydrogel scaffolding of transplanted GRPs in conjunction with serial *in vivo* imaging of cell survival and hydrogel degradation has potential for further advances in glial cell therapy.

Graphical Abstract

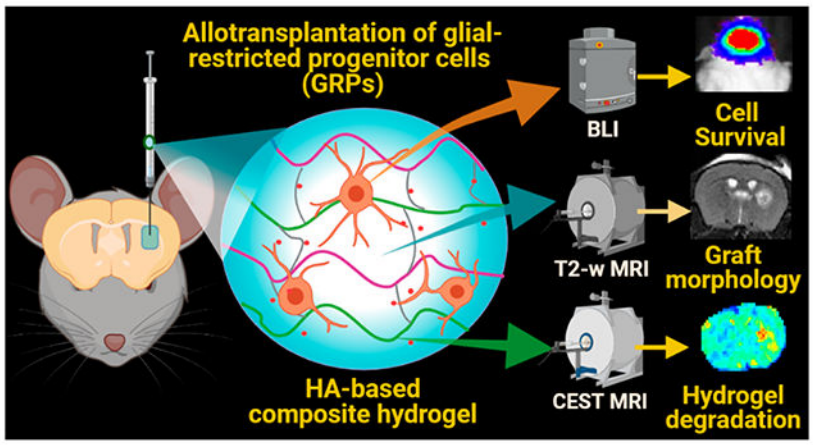

Keywords

glial-restricted progenitor; CEST MRI; BLI; hydrogel; biodegradation; gelatin; hyaluronic acid

1. INTRODUCTION

Neurodegenerative disorders including amyotrophic lateral sclerosis (ALS), stroke, and multiple sclerosis (MS) are characterized by inflammation and/or severe astrogliosis leading to neuronal death.[1–3] Prevalent anti-inflammatory drugs impart only a partial recovery without triggering endogenous repair or a notable change in the actual disease course.[4,5] Since the degenerating tissues of the central nervous system (CNS) lack the ability to robustly regenerate themselves, cell-based therapies for glial replacement are now being investigated to protect neurons and mitigate tissue atrophy.

In recent years, fetal-derived glial-restricted progenitors (GRPs) have shown promising potential to treat severe CNS degeneration.[6–8] Considering the lack of trophic support, rapid neuronal death, and the long timeline of remyelination (>3 months), it is critical to ensure a high degree of transplanted cell survival.[6,9] We previously observed that transplanted stem cell survival can be notoriously poor within a harsh *in vivo* neurodegenerative environment such as encountered in animal models of ALS, which are characterized by reactive astrogliosis and chronic neuroinflammation.[10] Furthermore, it has been reported that >90% of transplanted cells can be lost within 1 week of transplantation owing to the mechanical stresses on the cell membrane caused during injection, cell handling, hypoxia, and rapid immune rejection.[11,12]

To mitigate some of the encountered issues in cell therapy, cells have been scaffolded in injectable hydrogels which can not only protect cells from an initial host immune response but also shield cells from shear stress during harvest and injection.[13,14] It is essential to tune the hydrogel mechanics based on the injection conditions, nature of the transplanted cells, and the host *in vivo* conditions.[15] Hydrogel design should ensure structural support with sufficient binding sites, adequate nutrient diffusion, and a proper mechanical framework as well as biological support for cell adhesion, proliferation,

and differentiation.[16,17] Based on target tissue mechanics and the complexity of a local inflammatory microenvironment, peptide-, carbohydrate-, natural polymer- and synthetically cross-linked precursor-based gels with “click chemistry” designs are continually optimized to maximize the efficacy of cell therapy.[17–19] For nervous tissue regeneration, soft hydrogels having a ~50–500 kPa stiffness are believed to be optimal, prepared from self-assembling peptides, polyethylene glycol, methacrylate, or natural polymers (e.g., gelatin, hyaluronic acid, methylcellulose, and fibrin).[17,20] Although several scaffolds support cell viability, nervous tissue repair strategies necessitate the use of natural matrices which fulfill six critical requirements: injectability, biocompatibility, biodegradability, interactivity, porosity, and lack of swelling.[17,20,21] Ideally, shear thinning hydrogels provide a favorable mechanical support for cell transplantation by redistributing the shear forces away from the cells.[22,23] Since hyaluronic acid (HA) is abundantly present in the CNS, engineering injectable HA-based gel formulations with controllable chemistry and rheology is well suited for cell transplantation to the CNS. HA-based gels are also biodegradable and reduce glial scar formation.[18,24]

When employing these hydrogels, it is highly desirable to track their *in vivo* biodegradation and clearance to ensure graft safety and to allow biological tissue integration of transplanted cells. We combined thiol-modified HA (HA-S) with thiol-modified gelatin (Gel-S) to take advantage of the collagenous matrix of gelatin, which naturally contains abundant amide ($-NH_2$) groups and arginine–glycine–aspartic acid (RGD) motifs, which are vital for cell attachment and viability.[25,26]

In addition, the Gel-S component is biodegradable and an excellent source of endogenous chemical exchange saturation transfer magnetic resonance imaging (CEST MRI) contrast due to the presence of abundant amide protons exchanging with the surrounding water protons. The CEST contrast is specific for the saturation pulse applied at a characteristic frequency and can be exploited for imaging of chemical proton species such as the amide ^1H protons in gelatin. The continuous transfer of ^1H protons, when saturated by a characteristic radiofrequency pulse, leads to a “build-up” of saturated bulk water protons, causing a measurable decrease in the ^1H MRI signal. Hence, CEST MRI can directly report on hydrogel degradation *in vivo* without the need for using exogenous labels.[27,28] The Gel-S component was reacted with HA using a Michael-type thiol-acrylamide addition reaction with homo-bifunctional poly(ethylene glycol)diacrylate (PEGDA) as the cross-linker. This strategy allows *in situ* cell scaffolding with sufficiently slow gelling kinetics to allow for a proper time window of injection.[29–32]

Past studies have extensively focused on using HA hydrogels for scaffolding human stem cells in a xenogeneic transplantation paradigm, necessitating strict immunosuppression regimens which not only affect the natural host immune response against the graft but also against the scaffolding materials. Although allotransplantation of neural and glial progenitor cells with HA hydrogels has been performed in both small and large animal models,[21,33] non-invasive tracking of allografted cell fate in terms of proper graft placement, cell survival, differentiation, and host anti-graft immune response has not been fully explored. Moreover, in parallel with *in vivo* cell survival assessment, non-invasive monitoring of transplanted hydrogel degradation has not been explored despite its importance in ensuring

successful cell integration and clinical safety. In this study, we tuned the hydrogel mechanics to achieve optimal scaffolding and injection of transgenic GFP^+ mouse (m)GRPs transduced with the Luc2 reporter gene, allowing serial *in vivo* imaging of both cell survival and hydrogel degradation using bioluminescent imaging (BLI) and CEST MRI, respectively. Using an allogeneic donor/immunocompetent host transplantation paradigm, we report here on a comparison of HA hydrogel-scaffolded versus non-scaffolded (naked cells) cells in terms of *in vivo* cell survival, proliferation, differentiation, and hydrogel biodegradation. A schematic outline of our study is shown in Figure 1.

2. EXPERIMENTAL SECTION

2.1. Hydrogel Preparation and Characterization.

Composite HA hydrogel formulations were prepared by dissolving and mixing of lyophilized thiolated (HA-S and Gel-S) and thiol-reactive PEGDA components (ESI BIO Stem Cell Solutions, Alameda, CA) in degassed and deionized DNAse free water (pH = 7.0) at 25 °C. Briefly, the thiolated precursors were diluted, mixed, and incubated in a 37 °C water bath to promote gradual liquefaction before the addition of PEGDA. Component concentrations (% w/v diluent) were varied by altering the dilution in water to obtain composite hydrogel formulations from 5 to 20 mg/mL with varying gelation times and stiffnesses (Figure 2). In all four formulations, a constant (HA-S + Gel-S) to PEGDA volume ratio of 4:1 was maintained. The stiffness of the resulting composite hydrogels of different gelation and stiffness properties were characterized by small strain amplitude oscillatory rheology using a parallel-plate AR-G2 rheometer (TA Instruments, DE). A 25 mm stainless steel plate was secured in a humid chamber at 37 °C with a 0.5 μm gap width. At 1% constant strain and 1 Hz frequency, dynamic oscillatory strain measurements were performed within the moisture trap ($n \geq 4$ per hydrogel group). The gelation time of the prepared composite hydrogels was determined by placing a microhematocrit glass capillary tube (Thomas Scientific, NJ) on the surface of the hydrogel in 2 min intervals post mixing until the composite hydrogel mixture column ceased to rise in the tube. The degree of hydrogel swelling was determined after complete gelation of the composite hydrogel (200 μL) in 0.5 mL Eppendorf tubes by incubation with 1× phosphate-buffered saline (PBS) at 37 °C and the dried hydrogel was weighed at 0, 10, and 20 h. Swelling ratio (SR) was calculated as SR (%) = $[(W_s - W_o)]/W_o \times 100$, where W_s and W_o are weights of the dry hydrogel blocks ($n = 4$ per group) before and after incubation in saline. The mesh sizes (ξ) of the composite hydrogels were calculated from Flory—Rehner's theory as listed in Supporting Information Table S2. To assess hydrogel cross-linking, Fourier transform infrared spectroscopy (FTIR) was performed on the lyophilized precursors and cross-linked hydrogels using a ThermoNicolet Nexus 670 FTIR Spectrometer (GMI, Ramsay, MN). FTIR spectra were collected for a wavelength range of 4000–600 cm^{-1} in transmission mode with 256 scans. The ultrastructural morphology of the cross-linked hydrogels was assessed with a high-resolution scanning electron microscope equipped with a low vacuum detector at 2 kV (Prisma E SEM, Thermofisher, Waltham MA).

2.2. mGRP Culture.

A2B5$^+$ mGRPs were extracted from the fetal forebrain tissue of mid-gestation (E13) transgenic mice carrying the proteolipid protein-green fluorescent protein (GFP) gene. Cells were further transduced with a lentiviral vector carrying firefly luciferase (pLenti4-CMV-Luc) and positive clones were selected for hygromycin B (50 μg/mL) resistance to make stable cell lines. Cells were expanded in T75 cell flasks pre-coated with poly-L-lysine (Sigma, St. Louis, MO) and laminin (Life Technologies, Buffalo, NY) in a humidified atmosphere at 5% CO_2 at 37 °C. Cells were grown in serum-free Dulbecco's modified Eagle's-F12 medium (Life Technologies) supplemented with 1 mg/mL bovine serum albumin (Sigma), 0.1 mg/mL basic fibroblast growth factor (Cell Signaling Technology, Danvers, MA), B-27, N2, and penicillin (Life Technologies).

2.3. Assessment of *In Vitro* Cell Morphology, Proliferation, and Cell Survival.

In vitro assessment of cell behavior and survival with and without hydrogel scaffolding was performed in 48-well plates by seeding 4×10^3 cells/well in 45 μL with at least four wells for each composite hydrogel type, or PBS, respectively. For cell scaffolding, mGRP cell pellets were gently triturated in precursor solution (Gel-SH and HA-SH) followed by addition of PEGDA. Following gelation, 500 μL of medium was added. The medium was changed after 2 h to clear any un-reacted components, unattached cells, or cell debris, followed by a medium change after overnight incubation. Subsequent medium changes were performed during alternate days. The cell area of single cells was determined by setting a boundary threshold on ImageJ on the 20× phase contrast images with at least six regions of interest (ROIs) in four separate images per scaffolded or non-scaffolded cell group fixed with 4% paraformaldehyde (PFA) on day 4. *In vitro* proliferation of mGRPs was assessed by a Cell Counting Kit-8 (CCK-8) assay (Dojindo Molecular Technologies, Rockville, MD) at specific time intervals as per the manufacturer's protocol. In parallel with cell proliferation, mGRP cell viability was assessed by BLI of the culture plate by adding D-luciferin (15 μg/mL) in 10 mM PBS (pH = 7.4). Cells were imaged using an IVIS Spectrum/CT optical imaging instrument (Caliper Life Sciences, Hopkinton, MA) equipped with a highly sensitive, cryogenically cooled, charge-coupled device detection system.

2.4. Assessment of Injected *In Vitro* Cell Survival.

To assess the influence of injection on mGRP cell viability, two sets of 48-well cell culture plates were prepared in which mGRPs at a density of 2×10^6 cells/mL in composite hydrogel or PBS were passed through a 31G Hamilton syringe (Hamilton, Reno, NV) at 0.5 μL/min. One set of cell plates was used to perform *In vitro* BLI. To assess the percentage of the cells that did not survive the injection-induced stress, live/dead imaging was performed on another set of cell plates using a live/dead cell staining kit (Life Technologies, Carlsbad, CA), followed by fluorescent imaging using a Zeiss AX10 microscope. Cell death post injection was assessed by obtaining BLI readouts (as described in Section 2.3) and cell counting (using ImageJ) on a minimum of 5 live/dead images per group captured at 20× magnification with at least three fields of view.

2.5. CEST MRI Studies of *In Vitro* Hydrogel Degradation.

In vitro CEST MRI was performed at 37 °C on a 11.7 T horizontal Bruker AVANCE system (Bruker Biosciences, Billerica, MA) fitted with a 15 mm birdcage coil. Hydrogel phantoms ranging from 0.5 to 20 mg/mL were prepared and CEST images were obtained with a rapid acquisition and relaxation enhancement (RARE) readout and a quantitation of exchange using the saturation power method with a saturation pulse of B_1 = 3.6 μT at saturation offsets between −6.0 and +6.0 ppm. Other imaging parameters were slice thickness = 1.5 mm, number of averages (NA) = 2, echo time (TE) = 5 ms, repetition time (TR) = 5500 ms, matrix size = 64 × 64, field of view (FOV) = 16 × 10 mm^2, and RARE factor = 32. CEST contrast was calculated as $MTR_{asym} = \{S_{sat}(-\Delta w) - S_{sat}(\Delta w)\}/S_0$, where $S_{sat}(-\Delta w)$, $S_{sat}(-\Delta w)$, and S_0 represent the water signal with saturation frequency offsets at $-\Delta w$, Δw, and without saturation, respectively. For the degradation assay, a 10 mg/mL hydrogel formulation was prepared, which was incubated with 1 mg/mL collagenase (*Clostridium histolyticum* type IV, Sigma, St. Louis, MO) at 37 °C. At each time point, the enzyme solution was replenished after washing the sample twice with 1× PBS for 5 min, and CEST MRI was performed at 3.6 ppm using the above imaging parameters.

2.6. Animal Surgery and Cell Transplantation.

All animal procedures were performed on 8–12-week-old male immunocompetent BALB/c mice (Jackson laboratories, Bar Harbor, ME) under a protocol approved by our institutional animal care and use committee. Mice were anesthetized with 1.5% isoflurane during surgery. An s.c. injection of $1 \times 10_5$ cell mGRPs per dorsal site (n = 5) in 50 μL of either hydrogel formulation or PBS was given using a 28G needle syringe. Using a stereotaxic apparatus (Stoelting Co., Wood Dale, IL), cells were injected into the right brain striatum (n = 8) after exposing the skull with a 0.5 mm skull incision followed by drilling of a burrhole. 1.6 million mGRPs were mixed in either 20 μL of hydrogel precursor solution or PBS and subsequently transferred to a 10 μL Hamilton syringe attached to a 31G microinjection needle. Striatal injection (AP = 0 mm; ML = 2.0 mm; DV = 3.0 mm) of 2.5 μL of cell formulation at 0.5 μL/min was initiated at 5 min before hydrogel gelation, with the needle staying in place until 4 min post injection to minimize backflow.

2.7. BLI Studies of *In Vivo* Cell Survival.

Imaging was performed under 1–2% anesthesia. Serial *in vivo* BLI was performed at several time points post transplantation using an IVIS Spectrum/CT instrument. D-luciferin was given intraperitoneally at 150 mg/kg and BLI readouts were collected at 10, 15, 20, 25, and 30 min post luciferin injection. Luminescent images were captured at an exposure time of 1 min and peak emission values were recorded for the quantification of viable Luc^+ mGRPs using LIVINGIMAGE software (v 4.5.5, Caliper Life Sciences). For signal quantification, the photon signals were expressed in units of maximum photons per second per square centimeter area per steradian (photons/sec/cm^2/sr), measured from a defined region of interest with a fixed dimension, profile, and position for the whole experiment.

2.8. T_2-Weighted MRI and CEST MRI Studies of *In Vivo* Hydrogel Morphology and Biodegradation.

MRI was performed on a 11.7 T horizontal bore Bruker AVANCE scanner equipped with a 15 mm birdcage transmit/receive coil using a RARE pulse sequence. Imaging parameters were: slice thickness = 1.5 mm, NA = 2, TE = 19 ms, TR = 1500 ms, matrix dimensions = 128 × 128, FOV = 17 × 17 mm^2, and RARE factor = 16. For CEST imaging, a saturation power of B_1 = 3.6 μT was used with offset sampling from −5.5 to 5.5 ppm. MTR_{asym} values from a fixed ROI area (drawn by hand on day 1 and copied to all other time points) were calculated as described above and CEST contrast maps were derived via MATLAB (Mathworks, Natick, MA) program.

2.9. Postmortem Histology and Immunophenotyping.

Animals were sacrificed at 4 weeks post mGRP transplantation. Transcardial perfusion was performed via a controlled circulation of 5% sucrose followed by 4% PFA (Sigma, St. Louis, MO) in PBS. Brains were extracted and stored in 4% PFA overnight. Next, the brains were transferred to 30% sucrose for 48 h and cryopreserved at −80 °C until cryo-sectioning (tissue slice thickness = 20 μm). Overall histomorphological assessment was made by H&E staining. Immunohistochemistry was performed by blocking tissue sections first with 5% bovine serum albumin and 0.1% Triton X-100 (Sigma-Aldrich, St. Louis, MO) in Tris-buffered saline (TBS) for 1 h followed by incubation with primary antibodies overnight at 4 °C. Primary antibodies used were rabbit anti-Iba-1 (1:500, Wako, Japan), rabbit anti-GFAP (1:500, Dako, Z0334, USA), rabbit anti-Ki67 (1:250, Abcam, ab15580, MA), rabbit anti-GFP (1:300, Abcam, ab290, MA), and rabbit anti-Olig-2 (1:300, AB9610, Millipore, MA). Secondary antibodies used were goat anti-mouse, goat anti-rat, or goat anti-rabbit Alexa-Fluor 594 (1:1000, Thermofisher) and goat anti-rabbit Alexa-Fluor 647 (1:500, Thermofisher), incubated for 2 h on the following day after washing off the primary antibodies in 1× TBS, pH = 7.0. Immunocytochemical analysis of hydrogel-scaffolded and naked mGRPs were performed at days 4 and 16 of *in vitro* culture, using the antibodies listed in the Supporting Information Table S3). Histochemical and immunofluorescent images were acquired using a Zeiss Apotome 2 fluorescent microscope.

2.10. Statistical Analysis.

Statistical significance was analyzed using GraphPad Prism (version 8.0.2, GraphPad Software, San Diego, CA). Comparisons among multiple data groups were performed by one-way analysis of variance with Tukey's post hoc test. Pair-wise comparisons of the means were performed with a two-tailed Student's *t*-test.

3. RESULTS AND DISCUSSION

3.1. Optimization of Hydrogel Gelation and Characterization of Rheological Properties.

Hydrogels of variable mechanical strengths were obtained by reacting the thiolated HA-S, and Gel-S with the PEGDA cross-linker in a Michael-type addition at room temperature (Figure 2a). HA-S and PEGDA are vital for stable gelation as they affect the structural integrity of the hydrogel, with PEGDA being essential for complete cross-linking of the

components via a thiol-acrylamide linkage.[25] HA is the primary backbone of the brain extracellular matrix (ECM) and is degradable by the hyaluronidases produced by neurons/glial cells.[34,35] Similarly, gelatin-rich micro-niches provide ample cues for cell attachment and proliferation due to the presence of RGD sequences.[36] We previously showed that the RGD-rich Gel-S component of the hydrogel is highly essential for cell survival and is enzymatically degradable.[25] Moreover, the Gel-S component contains multiple amide protons that are exchangeable with the surrounding water protons, resulting in a CEST contrast at 3.6 and 1.8 ppm offset of water as clearly observed on the Z-spectra of individual components. These peaks were not present for the HA-S and PEGDA components, indicating the specificity of CEST MRI to image Gel-S as a label-free indicator of hydrogel degradation (Figure 2b).

In this study, our composite hydrogel design was aimed to ensure post-gelation stability by rapid, non-toxic thiol—ene based covalent cross-linking (via PEGDA) of both HA-S and Gel-S components and flexible tuning of hydrogel mechanics either by altering the mixing ratio or by differential dilution of the lyophilized constituents. While maintaining an HA-S/Gel-S/PEGDA ratio of 2:2:1, we performed dilution of all components in water to obtain a wide range of concentrations from 5 to 20 mg/mL (Supporting Information Table S1). The Michael-type thiol addition has been reported to have negligible byproduct formation.[37,38] We maintained a stoichio-metrically defined 2:1 molar ratio of thiols: double bonds for both thiolated precursors to ensure a reproducible 100% cross-linking efficiency.[39] We previously validated the lack of noncross-linked byproducts by pre-conjugating Gel-S and HA-S with maleimide-based near-infra-red (NIR) dyes, which, upon cross-linking via PEGDA, gelled within the same time frame as the non-labeled precursors without forming any unbound residues/byproducts as validated by NIR imaging.[28]

Immediately after mixing the precursors with PEGDA, the gelation time was monitored, with the 5 mg/mL composite hydrogel showing the longest time (>40 min) for complete gelation, while for 20 mg/mL, the gelation occurred within <15 min (Figure 2c). This trend indicated a concentration-dependent cross-linking progression and controllable gelation, which is essential to optimize the injection time window ahead of *in situ* gelation. In ionic solutions, HA hydrogels are known to exhibit ion-dependent swelling as per their innate pore morphology and water holding capacity.[40,41] We tested hydrogel swelling at a physiological pH of 7.0 and 37 °C by incubating fully cross-linked composite hydrogels in PBS for 10 and 20 h and noticed an increase in swelling with a decrease in component concentrations (Figure 2d). A significant swelling of >8% was observed at a 5 mg/mL concentration while in the remaining three groups, the swelling did not increase beyond ~4%. The rheological strain tests indicated that under a constant strain of 10%, the composite hydrogels showed an increased stiffness with increasing component concentrations, as evidenced by the increase in dynamic storage modulus (G') values from a minimum of 12 Pa at 5 mg/mL to a maximum of 700 Pa at 20 mg/mL (Figure 2e,f). Past studies have used hydrogels around a wide stiffness range of ~50—500 Pa for neural tissue engineering purposes.[20,42,43] These results indicate that the gelation and the stiffness properties can be conveniently varied by altering the concentrations of composite hydrogel components in a wide concentration range between 5 and 20 mg/mL. These stiffness values lie within the injectable range (10–1000 Pa) and in accordance with the elasticity modulus of

brain tissue (0.1–1 kPa).[44,45] FTIR analysis revealed the presence of gelatin-specific amide peaks from C═O stretching at ~1630 cm^{-1} and N–H bending ~1565 cm^{-1} in both Gel-S and the cross-linked hydrogel at 1565 cm^{-1} indicated a high density of amide functional groups (Figure S1). The disappearance/merging of sharp vibration peaks characteristic of PEGDA in the cross-linked hydrogel indicates that complete cross-linking was achieved. The ester peak at 1730 cm^{-1} specific to PEGDA was absent in the cross-linked hydrogel, further validating the successful cross-linking, with no residual carboxyls. Finally, the shifting of peaks toward the characteristic C–O stretching vibration peaks at ~1100 cm^{-1} and the C–H band stretching vibration peak at ~2866 cm^{-1} of PEGDA is in agreement with such complete cross-linking. Morphological characterization of dry hydrogels revealed a porous architecture with regular honeycomb-like pores decreasing in size and forming denser clusters with increasing hydrogel concentrations (Figure S1).

3.2. Effect of Hydrogel Scaffolding on the Morphology and Viability of mGRPs.

The stiffness and the mesh network of hydrogels influence the morphology of scaffolded cells and thereby their ability to proliferate and migrate within the 3D porous matrix.[46,47] By virtue of the dual expression of the Luc and GFP transgenes, we were able to determine cell survival and postmortem cell fate by BLI and fluorescence imaging, respectively. We first studied the morphology of the scaffolded mGRPs in all hydrogel formulations and observed differential cell shapes (Figure 3a) in response to variations in hydrogel stiffness. For a quantitative comparison, we estimated the cell areas within a fixed field of view and observed an increase in the cell spread area with decreasing component concentrations, indicating a stiffness-dependent cell anchorage (Figure 3b). Considering the stark differences in material properties between 2D tissue culture plates (TCP) and 3D hydrogels, the cell morphologies in these substrates were not compared. A higher cell anchorage, spreading, and cell motility are known to be supported by the 3D microenvironment of softer hydrogels.[47,48] Assessment of proliferation of scaffolded mGRPs expressed as percentage of cells using a calibration curve (Figure S3) showed a progressive trend throughout days 3, 5, and 7 post cell-seeding, where the softer hydrogels (5 and 10 mg/mL component concentrations) showed significantly enhanced proliferation compared to the TCP control (Figure 3c). On day 7, the 10 mg/mL hydrogels showed maximum proliferation as compared to other groups ($p < 0.05$). Overall, these differential cell proliferation rates are in response to differences in their local microenvironment and porous architecture (Figure S1). Compared to flat TCP surfaces and stiff hydrogels, the high mesh-like architecture with liquid (water/cell media) swollen polymeric networks within softer hydrogels is known to facilitate cell anchorage, division, and nutrient exchange.[47,48] Additionally, 3D cultures in soft hydrogels mimic the natural ECM of cells which favor longterm cell viability by reducing steric hindrance of ECM proteins and cell integrins and improving the interaction with the cells. In contrast, 2D cell cultures provide limited structural support cues which hinder cellular physiological functions beyond a certain threshold. The increased cell viability supported by the hydrogel scaffolds was further confirmed by *in vitro* fluorescence imaging of GFP^+ cells and BLI, with both showing an increasing proliferation after cell scaffolding. Post day 7, large GFP^+ cell clusters having a size of ~100 μm were observed (Figures 3d and S2).

Next, we assessed the increase in cell numbers with *in vitro* BLI. The BLI signal intensity showed a linear increase with the mGRP cell number (R^2 = 0.989, Figure 4a). In agreement with the proliferation rates, we noted higher BLI readouts for softer gels (≤15 mg/mL) with an elevated signal readout post day 5 (Figure 4b,c). The control (2D) substrates showed high BLI readouts on day 1, possibly due to a higher cell anchorage and direct access to growth medium compared to scaffolded cells. However, the readout of the control was reduced over time, and we observed cell overcrowding and partial detachment of cell layers from the culture plate surface (data not shown). The cell overcrowding on a 2D surface can cause contact inhibition affecting cell–cell and cell–matrix signaling, leading to an overall reduction of cellular metabolism.[49] For the scaffolded mGRPs, the Gel-S-based 3D microenvironment having anchorage-supportive RGD domains may cause an increasing trend in cell viability post day 5. The 10 mg/mL samples showed the highest cell number (BLI intensity) on day 7 (Figure 4d). Except for the stiff 20 mg/mL hydrogels, all other formulations showed enhanced cell numbers compared to the 2D control substrate, confirming the relatively higher survival of mGRPs in softer hydrogels. Based on the favorable *in vitro* survival properties, we chose 10 mg/mL hydrogels to further study the mGRP phenotypic expression in 3D cultures. On day 4 post cell seeding, hydrogel scaffolded mGRPs showed similar levels of biomarkers as the 2D cultures except for a higher $GFAP^+$ expression. On day 16, hydrogel-scaffolded mGRPs showed the presence of >70 μm cell clusters with high expression of characteristic glial progenitor biomarkers along with a higher level of the proliferation marker Ki-67 (Supporting Information Figures S4–S6).

3.3. Survival of Scaffolded and Naked mGRPs *In Vitro* during the Injection Procedure.

Since direct cell injection is known to induce cell death due to shear-induced stress, we tested mGRP survival after passing them through a 31G needle syringe (“injected” at 0.5 μL/min) with and without hydrogel scaffolding against the same formulation undergoing manual pipetting (“pipetted”) with a 100 μL Eppendorf pipette (Figure 5a). For all formulations, a decreased BLI readout was observed for the injected group compared to the pipetted group (Figure 5b,c). However, a significant reduction ($p < 0.01$) in signal was observed for cells in saline in the injected group. We quantified the actual fraction of dead cells (% propidium iodide (PI) positive cells) in each group and found a significant correlation (R^2 = 0.946) with the BLI readout (Figure 5d,e). Both BLI and PI staining showed a high cell loss ($p < 0.001$) during cell injection with saline, which did not occur for cells scaffolded with the softer hydrogels.

One of the main factors determining the eventual graft performance after transplantation is the actual percentage of cells that survive cell harvest, transfer, and injection/catheter delivery procedures.[22,50] These pre-transplantation procedures can inflict significant cell death due to hypoxia and mechanical stress, which should be avoided especially when transplanting delicate primary cells such as fetal-derived GRPs.[14,19] For all hydrogel formulations, there was only a slight decrease in cell number post injection as compared to pipetted cells, while direct injection of mGRPs suspended in saline resulted in a loss of ~60% of harvested cells. Further, among all formulations, a notably high cell survival was seen for the softer hydrogels in a 40–300 Pa stiffness range. Hence, hydrogel scaffolding

with softer hydrogels (<15 mg/mL concentration) not only prevents injection-induced instant cell death compared to saline controls but, once transplanted, also provides a conducive 3D-microenvironment to support cell metabolism and growth. In line with this, a relatively higher post-injection survival was reported for cells encapsulated in shear thinning visco-elastic formulations compared to cells dispersed in non-cross-linked free solutions.[13,14,51]

3.4. CEST Imaging of Composite Hydrogels *In Vitro*.

The CEST properties of the composite hydrogels formulated with different degrees of stiffness were measured after complete cross-linking. The CEST Z-spectra (Figure 6a) and the MTR_{asym} spectra (Figure 6b) revealed a major peak at 3.6 ppm and a relatively smaller peak at 1.8 ppm characteristic of the abundant amide protons of the Gel-S component. These results were in agreement with Gel-S (only) phantoms and the composite hydrogels studied with varied Gel-S to HA-S ratios. Although we maintained a constant Gel-S to HA-S ratio of 1:1, we observed an increased CEST contrast at 3.6 ppm when increasing the concentration from 5 to 20 mg/mL for all components (Figure 6c,d, $R^2 = 0.99$). Additionally, an increase in the broader peak between 0.5 and 2.0 ppm representing HA hydroxyl (−OH) protons was observed when the % wt % HA-S was increased. A distinguishable CEST contrast (signal to noise ratio: SNR > 8) was detected in all hydrogel formulations irrespective of their stiffness grades. Next, we tested the feasibility of CEST MRI to monitor the degradation of a 10 mg/mL hydrogel formulation, which showed optimal cell survival and proliferation. The hydrogel was incubated with 1 mU/mL collagenase which digests gelatins. The CEST signal was then serially measured for 2 weeks. A rapid decrease in CEST signal was detected as a result of hydrogel decomposition. At day 14, the contrast became nearly undetectable (Figure 6e,f). As this formulation conferred optimal cytoprotection, we chose a 10 mg/mL hydrogel for further *in vivo* applications.

3.5. Intracerebral Transplantation of Scaffolded Allogeneic mGRPs in Immunocompetent Mice.

Since most clinical scenarios require the use of immediately available, well-defined, thoroughly characterized, and standardized cell populations, the use of allogeneic grafts is the most practical approach. When using xenografts, that is, transplanting human GRPs in mice, one would need to use either inbred immunocompromised mouse strains or administer immunosuppressive drugs, both of which will affect the host immune response against the scaffolds. To complicate things further, hGRPs themselves can be immunosuppressive in a mouse model of MS.[52] In addition, there are species-specific differences in host brain tissue make-up and transplanted cell integration. We previously transplanted both mGRPs and hGRPs in dysmyelinated, immunocompromised shiverer mice and observed large species-to-species variations in the distance of cell migration and the extent of myelination.[8,53]

Allogenic transplantation of mGRPs has been successfully used in proof-of-concept studies in animal models of human leukodystrophy, stroke, and spinal cord injury. Recently, combining allogeneic transplantation of mGRPs with T-cell-suppressive antibodies has been reported to prolong transplanted cell survival in brain.[9] Despite persistent efforts in developing specialized cell lines for neuronal/glial cell replacement therapies, their clinical success is largely determined by their ability to survive and actively integrate at

the target tissues. Host immune rejection is a major limiting factor linked to immediate death of transplanted cells. To understand the robustness of scaffolded mGRPs, we assessed cell survival and immune reactivity in immunocompetent mice without administering any immunosuppression.

For dopaminergic neurons derived from embryonic neural precursors, a >50% cell loss after cell harvesting from 2D surfaces has been reported, demonstrating the need for immediate cytoprotection and emulation of their natural 3D niche.[19] Other studies have shown that even only a mere ~3—4 and ~1.6% of the initially xenografted cells survive after ~1.5 and ~4.5 months post transplantation in the CNS, respectively, even with immunosuppression.[19,26] Furthermore, within a highly inflammatory and hypoxic environment such as the ischemic brain, a twofold increase in survival of NPCs was shown after HA scaffolding.[26] We observed an overall cell survival of ~6.8% of the originally transplanted cells at day 32 with hydrogel scaffolding, which accounts for a 4.5-fold increase in survival compared to naked cells (Figure 7).

Allografts of GRPs and NPCs scaffolded in hydrogels and implanted in the canine[21] and rat[26,33] CNS showed safe embedding of cells. However, the long-term cell survival and host immune reaction have not been adequately explored. Here, monitoring of transplanted cell fate using serial *in vivo* imaging is important not only for assessing initial cell death but also to design early therapeutic intervention for safe graft integration and to mitigate any tumorigenesis.

To simultaneously assess *in vivo* cell survival of hydrogel-scaffolded mGRPs for different hydrogel formulations, we performed subcutaneous (s.c.) injection of the graft at multiple dorsal sites in immunocompetent BALB/c mice followed by BLI up to 9 days (Figure S7). On day 9, regardless of the hydrogel formulation, a relatively higher BLI readout was seen for hydrogel-scaffolded Luc^+ mGRPs as compared to naked cells suspended in saline (control). In agreement with the *in vitro* results, the mGRP scaffolds in softer (10 and 5 mg/mL) formulations showed the highest BLI intensity compared to the other groups on day 9. Based on the relative ease of injection, average gelation time, and high cytocompatibility, we decided to use the 10 mg/mL hydrogel as the optimal formulation to further assess post-transplantation survival of scaffolded mGRPs in mouse brain. Next, we monitored the survival of scaffolded versus naked mGRPs transplanted in brain striatum with serial BLI up to 32 days post injection (Figure 7d,e). After 2 h post-surgery, peak readouts were recorded and set as the value for day 0, to which the BLI readings for subsequent time points were normalized. The BLI signal gradually decreased over 32 days in both groups, but the decrease was significantly higher in the saline group post day 7 ($p < 0.05$); the number of surviving cells was 4.5-fold higher in the hydrogel group at the end point of BLI.

3.6. CEST MRI of Composite Hydrogel Degradation *In Vivo*.

T_2-weighted MRI and CEST MRI were conducted concurrently with BLI over a period of 32 days. T_2-weighted MRI was performed first in order to localize the hydrogel injection site in the brain striatum anatomically. A hyperintense T_2-*w* signal could be identified at the injection site owing to the higher water content within the hydrogel matrix, which showed a reduction in size over time (Figure 8a). T_2-*w* imaging itself is not specific for the hydrogel

as the signal is derived from unbound water protons in the hydrogel, which can be affected by volumetric changes due to hydrogel swelling/shrinking in the host tissue. In contrast, the CEST signal is specific for the exchangeable protons within the hydrogel. The *in vivo* MTR_{asym} spectra revealed two peaks at 0.5–2.0 and 3.6 ppm, which were also detected for the *in vitro* phantoms (Figure 8b). Only at the hydrogel injected site did the CEST MTR_{asym} values at 3.6 ppm show a progressive decrease over 32 days (Figure 8c). There was no CEST contrast at the injection site for the saline control group (naked mGRPs). In comparison to the *in vitro* CEST phantom studies, a higher peak was seen *in vivo* at 0.5–2.0 ppm, which can be attributed to the complex *in vivo* tissue microenvironment rich with intracellular and extracellular matrix peptide, carbohydrate, and metabolite constituents. Nevertheless, the CEST spectra are in agreement with previous *in vivo* CEST studies on composite HA hydrogels without cells.[27] Importantly, in this study, we noted that the presence of mGRP cells in the hydrogel scaffold (or saline control) did not significantly alter the CEST spectra showing negligible contrast at 3.6 ppm supporting the specificity of CEST MRI for the abundant exchangeable amide protons in gelatin.

3.7. Immunohistological Assessment of Graft Morphology, Cell Differentiation, and Host Immune Response.

Postmortem hematoxylin & eosin (H&E) staining revealed a dense region of transplanted cells in the hydrogel matrix (Figure 9a,a′). Grafted cells could be clearly distinguished from the surrounding tissue due to their GFP^+ fluorescence (Figure 9b,c,c′), with the ipsilateral region showing the presence of $Iba1^+$ cells around the transplanted cells (Figure 9b′). As an additional validation, GFP^+ mGRPs at the transplant site were characterized by anti-GFP antibody staining, which showed co-localization with the transplanted cells (Figure 8d–d‴). Next, we assessed the host immune response against scaffolded versus naked mGRPs. Compared to naked cells, there was a significant decrease ($p < 0.05$) in the number of activated ($Iba1^+$) microglia/macrophages present in and around the hydrogel scaffolded mGRP graft region (Figure 9e–g′,k). Irrespective of the presence of mGRPs in the hydrogel, $GFAP^+$ astrocytes were confined at the boundary of the hydrogel, forming a ~30 μm glial scar layer (Figure 9h–j). For naked cells, a higher $GFAP^+$ cell area was measured, indicating a direct reactivity of activated native astrocytes toward the transplanted mGRPs (Figure 9m). The relatively higher GFP^+ cell area for the hydrogel scaffolding further supports a protective role for the hydrogel scaffold (Figure 9l). Autofluorescence from non-cellular components of the graft was carefully identified and accounted for (Figure S8).

Assessment of mGRP graft morphology by H&E staining showed that injecting the formulation at ~22 min post-crosslinker (PEGDA) addition was optimal for *in situ* gelation and restricted localization. Scaffold implantation within the CNS may be associated with a host immune reaction which can limit its intended application.[54] Maximum microglial response and astrocytic activity around the scaffold is known to occur by 7–14 days post transplantation and can persist for over 3–4 weeks in certain cases.[55–57] Specifically, striatal allografts can be heavily infiltrated with T cells and macrophages/microglia as early as 2 weeks post transplantation in immunocompetent mice.[58] The hydrogel itself (without cells) may also cause glial scarring at the tissue—scaffold interface, forming a barrier of activated astrocytes. Post 14-day transplantation, we saw that the presence of activated microglial cells

was highly restricted at the hydrogel boundary, indicating that hydrogel scaffolding may act as a barrier for infiltrating immune cells. The decreased microglial (Iba-1) activation can be attributed to the general low immunogenicity of HA, even in the highly inflammatory environment of the ischemic brain.[32] However, a stiffness (storage modulus) increase >100 Pa may significantly increase astrocytic activation.[32,59] Moreover, low-molecular-weight HA species (<10 kDa) are known to induce astrocyte activation even with thiol modification and, with increased precursor size, are associated with an increased mesh size.[32,60] In this study, the use of a thiolated-HA species of 300 kDa and a composite formulation of <100 Pa resulted in a reduced astrocyte activation. Our mesh sizes of all hydrogel formulations ranged from 24.67 ± 3.1 to 125.45 ± 4.6 nm, which can allow optimal cell spreading and anchorage of cell processes and prevent penetration of infiltrating astrocytes or microglia, which range from 10 to 20 μm in size. The scaffolding may also support a sustained release of paracrine factors as the mGRPs may modulate local inflammation via trophic effects even without direct contact with the injured tissue.[61] A slight activation of local microglia may also trigger astrocyte-mediated neuroprotection for transplanted mGRPs resulting from an increased secretion of brain-derived neurotrophic factor, which aids in neurogenesis and myelination *in vivo*.[62,63] Eventually, the denuded axons can be protected from inflammation via the formation of intact myelin sheaths by differentiated $Olig2^+$ cells, which integrate in the host tissue as the hydrogel degrades. With increasing distance from the injection site, fewer activated astrocytes could be seen (Figure 9h′,j′). The hydrogel also causes re-modeling or local changes in the ECM around its boundary, which may trigger an immune response. Significant glial activation with large (activated) astrocytic cells was also seen in the case of saline-based mGRP injection, which indicates that allogeneic naked cells and cell debris can trigger a significant astrocytic response. Notably, despite the observed mild inflammation, our composite hydrogel conferred a high cytoprotection in the brain striatum, which led to an overall cell survival of ~6.8% of the originally transplanted cells (vs 1.47% of surviving naked cells) at day 32 in immunocompetent mice without administering any immunosuppression.

3.8. mGRP Phenotype and Proliferation.

At last, we assessed the expression of glial and oligodendrocytic markers by transplanted mGRPs at 4 weeks post transplantation. For the hydrogel-scaffolded mGRPs, a higher number of cells expressing the Olig2 biomarker was observed compared to the saline group (Figure 10a,d). As for GFAP expression, since the transplanted cells are also of murine (fetal) origin, we only quantified $GFAP^+$ cells that co-expressed GFP^+ cells to avoid counting host astrocytes. A higher number of dual $GFAP/GFP^+$ cells was observed compared to the saline group (Figure 10b,e). Enhanced astrocytic differentiation of allogeneic mGRPs is associated with pathological improvement in a mouse model of leukodystrophy.[64] Moreover, a gelatin matrix can upregulate GFAP expression, aiding in the formation of A2-like neurosupportive astrocytes.[65] At the end of 4 weeks, hydrogel-scaffolded mGRPs exhibited a significantly higher percentage of proliferating cells compared to the saline control as demonstrated by anti-Ki-67 staining (Figure 10c,f). This could be a result of the supportive 3D scaffold microenvironment offering multiple cell adhesion sites through the presence the Gel-S. Past reports have shown $Ki\text{-}67^+$ proliferation of HA-scaffolded iPSC-derived NPCs in the stroke cavity even at 6 weeks post

transplantation.[66] Approximately 13–14% of transplanted neuroepithelial cells were found to be still proliferative 9 weeks post injury with HA-methyl cellulose hydrogel scaffolding.[67] T_2-weighted MRI did not indicate any abnormal inflammation or tissue damage at the transplant site (Figure 8a).

4. CONCLUSIONS

We demonstrated that hydrogel biodegradation can be monitored with CEST MRI, with the hydrogel acting as a barrier for infiltrating host immune cells. In parallel, serial *in vivo* BLI revealed enhanced survival of transplanted Luc^+ allogeneic mGRPs in immunocompetent mice. As compared to naked cells, hydrogel scaffolding of transplanted mGRPs resulted in a 4.5-fold enhancement of cell survival, 1.62-fold enhancement of cell proliferation, and 2.12- and 2.75-fold enhancement of oligodendrocyte and astrocyte differentiation, respectively, *in vivo*. Hence, HA hydrogel scaffolding is well suited to prevent high initial allogeneic cell death in the immunocompetent CNS, which has been a major challenge in glial cell therapy for neurodegenerative disease. Implementing multi-modal/multi-parametric imaging including BLI, T_2-*w* MRI, and CEST MRI enables simultaneous, real-time monitoring of transplanted cell fate and hydrogel biodegradation *in vivo*, allowing a better assessment of the overall benefit of scaffolding cells in hydrogels.

Supplementary Material

Refer to Web version on PubMed Central for supplementary material.

ACKNOWLEDGMENTS

This work was supported by the National Institute for Health (NIH R01 EB023647) and the Maryland Stem Cell Research Fund (MSCRFD-3899 and MSCRFF-4250).

REFERENCES

(1). Miller DW; Cookson MR; Dickson DW Glial Cell Inclusions and the Pathogenesis of Neurodegenerative Diseases. Neuron Glia Biol. 2004, 1, 13–21. [PubMed: 16614753]

(2). Robel S; Buckingham SC; Boni JL; Campbell SL; Danbolt NC; Riedemann T; Sutor B; Sontheimer H Reactive Astrogliosis Causes the Development of Spontaneous Seizures. J. Neurosci 2015, 35, 3330–3345. [PubMed: 25716834]

(3). Skotte NH; Andersen JV; Santos A; Aldana BI; Willert CW; Nørremølle A; Waagepetersen HS; Nielsen ML Integrative Characterization of the R6/2 Mouse Model of Huntington's Disease Reveals Dysfunctional Astrocyte Metabolism. Cell Rep. 2018, 23, 2211–2224. [PubMed: 29768217]

(4). Yrjanheikki J; Tikka T; Keinanen R; Goldsteins G; Chan PH; Koistinaho J A Tetracycline Derivative, Minocycline, Reduces Inflammation and Protects Against Focal Cerebral Ischemia With a Wide Therapeutic Window. Proc. Natl. Acad. Sci. U.S.A 1999, 96, 13496–13500. [PubMed: 10557349]

(5). Zhu S; Stavrovskaya IG; Drozda M; Kim BYS; Ona V; Li M; Sarang S; Liu AS; Hartley DM; Wu DC; Gullans S; Ferrante RJ; Przedborski S; Kristal BS; Friedlander RM Minocycline Inhibits Cytochrome c Release and Delays Progression of Amyotrophic lateral sclerosis in mice. Nature 2002, 417, 74–78. [PubMed: 11986668]

(6). Walczak P; All AH; Rumpal N; Gorelik M; Kim H; Maybhate A; Agrawal G; Campanelli JT; Gilad AA; Kerr DA; Bulte JWM Human Glial-restricted Progenitors Survive, Proliferate,

and Preserve Electrophysiological Function in Rats with Focal Inflammatory Spinal Cord Demyelination. Glia 2011, 59, 499–510. [PubMed: 21264955]

(7). Almad AA; Maragakis NJ Glia: an Emerging Target for Neurological Disease Therapy. Stem Cell Res. Ther 2012, 3, 37. [PubMed: 23021042]

(8). Lyczek A; Arnold A; Zhang J; Campanelli JT; Janowski M; Bulte JWM; Walczak P Transplanted Human Glial-restricted Progenitors Can Rescue the Survival of Dysmyelinated Mice Independent of the Production of Mature, Compact Myelin. Exp. Neurol 2017, 291, 74–86. [PubMed: 28163160]

(9). Li S; Oh BC; Chu C; Arnold A; Jablonska A; Furtmüller GJ; Qin H-M; Boltze J; Magnus T; Ludewig P; Janowski M; Brandacher G; Walczak P Induction of Immunological Tolerance to Myelinogenic Glial-restricted Progenitor Allografts. Brain 2019, 142, 3456–3472. [PubMed: 31529023]

(10). Srivastava AK; Gross SK; Almad AA; Bulte CA; Maragakis NJ; Bulte JWM Serial In vivo Imaging of Transplanted Allogeneic Neural Stem Cell Survival in a Mouse Model of Amyotrophic Lateral Sclerosis. Exp. Neurol 2017, 289, 96–102. [PubMed: 28038988]

(11). Steele AN; MacArthur JW; Woo YJ Stem Cell Therapy: Healing or Hype? Why Stem Cell Delivery Doesn't Work. Circ. Res 2017, 120, 1868–1870. [PubMed: 28596172]

(12). Afreen S; Weiss JM; Strahm B; Erlacher M Concise Review: Cheating Death for a Better Transplant. Stem Cell. 2018, 36, 1646–1654.

(13). Aguado BA; Mulyasasmita W; Su J; Lampe KJ; Heilshorn SC Improving Viability of Stem Cells During Syringe Needle Flow Through the Design of Hydrogel Cell Carriers. Tissue Eng., Part A 2012, 18, 806–815. [PubMed: 22011213]

(14). Marquardt LM; Heilshorn SC Design of Injectable Materials to Improve Stem Cell Transplantation. Curr. Stem Cell Rep 2016, 2, 207–220. [PubMed: 28868235]

(15). Sarem M; Arya N; Heizmann M; Neffe AT; Barbero A; Gebauer TP; Martin I; Lendlein A; Shastri VP Interplay Between Stiffness and Degradation of Architectured Gelatin Hydrogels Leads to Differential Modulation of Chondrogenesis In vitro and In vivo. Acta Biomater. 2018, 69, 83–94. [PubMed: 29378326]

(16). Yip D; Cho CH A Multicellular 3D Heterospheroid Model of Liver Tumor and Stromal Cells in Collagen Gel for Anti-Cancer Drug Testing. Biochem. Biophys. Res. Commun 2013, 433, 327–332. [PubMed: 23501105]

(17). Fukunaga K; Tsutsumi H; Mihara H Self-Assembling Peptides as Building Blocks of Functional Materials for Biomedical Applications. Bull. Chem. Soc. Jpn 2019, 92, 391–399.

(18). Tian WM; Hou SP; Ma J; Zhang CL; Xu XY; Lee IS Hyaluronic Acid–Poly-D-Lysine-Based Three-Dimensional Hydrogel for Traumatic Brain Injury. Tissue Eng. 2005, 11, 513–525. [PubMed: 15869430]

(19). Adil MM; Vazin T; Ananthanarayanan B; Rodrigues GMC; Rao AT; Kulkarni RU; Miller EW; Kumar S; Schaffer DV Engineered Hydrogels Increase the Post-transplantation Survival of Encapsulated hESC-Derived Midbrain Dopaminergic Neurons. Biomaterials 2017, 136, 1–11. [PubMed: 28505596]

(20). Kornev VA; Grebenik EA; Solovieva AB; Dmitriev RI; Timashev PS Hydrogel-Assisted Neuroregeneration Approaches Towards Brain Injury Therapy: A State-of-the-Art Review. Comput. Struct. Biotechnol. J 2018, 16, 488–502. [PubMed: 30455858]

(21). Malysz-Cymborska I; Golubczyk D; Kalkowski L; Burczyk A; Janowski M; Holak P; Olbrych K; Sanford J; Stachowiak K; Milewska K; Gorecki P; Adamiak Z; Maksymowicz W; Walczak P MRI-Guided Intrathecal Transplantation of Hydrogel-Embedded Glial Progenitors in Large Animals. Sci. Rep 2018, 8, 16490. [PubMed: 30405160]

(22). Foster AA; Marquardt LM; Heilshorn SC The Diverse Roles of Hydrogel Mechanics in Injectable Stem Cell Transplantation. Curr. Opin. Chem. Eng 2017, 15, 15–23. [PubMed: 29085771]

(23). Wang Y; He X; Bruggeman KF; Gayen B; Tricoli A; Lee WM; Williams RJ; Nisbet DR Peptide Programmed Hydrogels as Safe Sanctuary Microenvironments for Cell Transplantation. Adv. Funct. Mater 2020, 30, 1900390.

(24). Wang X; He J; Wang Y; Cui F-Z Hyaluronic Acid-Based Scaffold for Central Neural Tissue Engineering. Interface Focus 2012, 2, 278–291. [PubMed: 23741606]

(25). Liang Y; Walczak P; Bulte JWM The Survival of Engrafted Neural Stem Cells Within Hyaluronic Acid Hydrogels. Biomaterials 2013, 34, 5521–5529. [PubMed: 23623429]

(26). Zhong J; Chan A; Morad L; Kornblum HI; Guoping Fan G; Carmichael ST Hydrogel Matrix to Support Stem Cell Survival After Brain Transplantation in Stroke. Neurorehabil. Neural. Repair 2010, 24, 636–644. [PubMed: 20424193]

(27). Liang Y; Bar-Shir A; Song X; Gilad AA; Walczak P; Bulte JWM Label-free Imaging of Gelatin-Containing Hydrogel Scaffolds. Biomaterials 2015, 42, 144–150. [PubMed: 25542802]

(28). Zhu W; Chu C; Kuddannaya S; Yuan Y; Walczak P; Singh A; Song X; Bulte JWM In Vivo Imaging of Composite Hydrogel Scaffold Degradation Using CEST MRI and Two-Color NIR Imaging. Adv. Funct. Mater 2019, 29, 1903753. [PubMed: 32190034]

(29). Phelps EA; Enemchukwu NO; Fiore VF; Sy JC; Murthy N; Sulchek TA; Barker TH; García AJ Maleimide Cross-linked Bioactive PEG Hydrogel Exhibits Improved Reaction Kinetics and Cross-linking for Cell Encapsulation and In situ Delivery. Adv. Mater 2012, 24, 64–70. [PubMed: 22174081]

(30). Hiemstra C; van der Aa LJ; Zhong Z; Dijkstra PJ; Feijen J Rapidly in Situ-Forming Degradable Hydrogels from Dextran Thiols through Michael Addition. Biomacromolecules 2007, 8, 1548–1556. [PubMed: 17425366]

(31). Hassan W; Dong Y; Wang W Encapsulation and 3D Culture of Human Adipose-Derived Stem cells in an in-situ crosslinked hybrid hydrogel composed of PEG-based hyperbranched copolymer and hyaluronic acid. Stem Cell Res. Ther 2013, 4, 32. [PubMed: 23517589]

(32). Lam J; Lowry WE; Carmichael ST; Segura T Delivery of iPS-NPCs to the Stroke Cavity within a Hyaluronic Acid Matrix Promotes the Differentiation of Transplanted Cells. Adv. Funct. Mater 2014, 24, 7053–7062. [PubMed: 26213530]

(33). Mothe AJ; Tam RY; Zahir T; Tator CH; Shoichet MS Repair of the Injured Spinal Cord by Transplantation of Neural Stem Sells in a Hyaluronan-Based Hydrogel. Biomaterials 2013, 34, 3775–3783. [PubMed: 23465486]

(34). Al'Qteishat A; Gaffney J; Krupinski J; Rubio F; West D; Kumar S; Kumar P; Mitsios N; Slevin M Changes in Hyaluronan Production and Metabolism Following Ischaemic Stroke in Man. Brain 2006, 129, 2158–2176. [PubMed: 16731541]

(35). Lindwall C; Olsson M; Osman AM; Kuhn HG; Curtis MA Selective Expression of Hyaluronan and Receptor for Hyaluronan Mediated Motility (Rhamm) in the Adult Mouse Subventricular Zone and Rostral Migratory Stream and in Ischemic Cortex. Brain Res. 2013, 1503, 62–77. [PubMed: 23391595]

(36). Sarker B; Singh R; Zehnder T; Forgber T; Alexiou C; Cicha I; Detsch R; Boccaccini AR Macromolecular Interactions in Alginate–Gelatin Hydrogels Regulate the Behavior of Human Fibroblasts. J. Bioact. Compat Polym 2017, 32, 309–324.

(37). Nair DP; Podgórski M; Chatani S; Gong T; Xi W; Fenoli CR; Bowman CN The Thiol-Michael Addition Click Reaction: A Powerful and Widely Used Tool in Materials Chemistry. Chem. Mater 2014, 26, 724–744.

(38). Su J. Thiol-Mediated Chemoselective Strategies for In Situ Formation of Hydrogels. Gels 2018, 4, 72.

(39). Zheng Shu X; Liu Y; Palumbo FS; Luo Y; Prestwich GD In Situ Crosslinkable Hyaluronan Hydrogels for Tissue Engineering. Biomaterials 2004, 25, 1339–1348. [PubMed: 14643608]

(40). Collins MN; Birkinshaw C Investigation of the Swelling Behavior of Crosslinked Hyaluronic Acid Films and Hydrogels produced Using Homogeneous Reactions. J. Appl Polym. Sci 2008, 109, 923–931.

(41). Zhou Z; Yang Z; Kong L; Liu L; Liu Q; Zhao Y; Zeng W; Yi Q; Cao D Preparation and Characterization of Hyaluronic Acid Hydrogel Blends with Gelatin. J. Macromol Sci., Part B: Phys 2012, 51, 2392–2400.

(42). Pakulska MM; Ballios BG; Shoichet MS Injectable Hydrogels for Central Nervous System Therapy. Biomed. Mater 2012, 7, 024101. [PubMed: 22456684]

(43). Jiang FX; Yurke B; Schloss RS; Firestein BL; Langrana NA Effect of Dynamic Stiffness of the Substrates on Neurite Outgrowth by Using a DNA-Crosslinked Hydrogel. Tissue Eng., Part A 2010, 16, 1873–1889. [PubMed: 20067396]

(44). Lou J; Liu F; Lindsay CD; Chaudhuri O; Heilshorn SC; Xia Y Dynamic Hyaluronan Hydrogels with Temporally Modulated High Injectability and Stability Using a Biocompatible Catalyst. Adv. Mater 2018, 30, 1705215.

(45). Engler AJ; Sen S; Sweeney HL; Discher DE Matrix Elasticity Directs Stem Cell Lineage Specification. Cell 2006, 126, 677–689. [PubMed: 16923388]

(46). Sun M; Chi G; Li P; Lv S; Xu J; Xu Z; Xia Y; Tan Y; Xu J; Li L; Li Y Effects of Matrix Stiffness on the Morphology, Adhesion, Proliferation and Osteogenic Differentiation of Mesenchymal Stem Cells. Int. J. Med. Sci 2018, 15, 257–268. [PubMed: 29483817]

(47). Ehrbar M; Sala A; Lienemann P; Ranga A; Mosiewicz K; Bittermann A; Rizzi SC; Weber FE; Lutolf MP Elucidating the Role of Matrix Stiffness in 3D Cell Migration and Remodeling. Biophys. J 2011, 100, 284–293. [PubMed: 21244824]

(48). Li X; Liu X; Cui L; Brunson C; Zhao W; Bhat NR; Zhang N; Wen X Engineering an in situ Crosslinkable Hydrogel for Enhanced Remyelination. FASEB J. 2013, 27, 1127–1136. [PubMed: 23239823]

(49). Balasubramanian S; Packard JA; Leach JB; Powell EM Three-Dimensional Environment Sustains Morphological Heterogeneity and Promotes Phenotypic Progression During Astrocyte Development. Tissue Eng., Part A 2016, 22, 885–898. [PubMed: 27193766]

(50). Wagner MA; Marks WH; Bhatia SK Hydrogel Encapsulation to Improve Cell Viability During Syringe Needle Flow. J. Long Term Eff. Med. Implants 2014, 24, 151–162. [PubMed: 25272214]

(51). Lopez Hernandez H; Grosskopf AK; Stapleton LM; Agmon G; Appel EA Non-Newtonian Polymer–Nanoparticle Hydrogels Enhance Cell Viability during Injection. Macromol. Biosci 2019, 19, 1800275.

(52). Kim H; Walczak P; Muja N; Campanelli JT; Bulte JWM ICV-transplanted Human Glial Precursor Cells are Short-lived Yet Exert Immunomodulatory Effects in Mice with EAE. Glia 2012, 60, 1117–1129. [PubMed: 22499166]

(53). Srivastava RK; Bulte JWM; Walczak P; Janowski M Migratory Potential of Transplanted Glial Progenitors as Critical Factor for Successful Translation of Glia Replacement Therapy: The Gap between Mice and Men. Glia 2018, 66, 907–919. [PubMed: 29266673]

(54). Meng F; Modo M; Badylak SF Biologic Scaffold for CNS Repair. Regen. Med 2014, 9, 367–383. [PubMed: 24935046]

(55). Das S; Zhou K; Ghosh D; Jha NN; Singh PK; Jacob RS; Bernard CC; Finkelstein DI; Forsythe JS; Maji SK Implantable Amyloid Hydrogels for Promoting Stem Cell Differentiation to Neurons. NPG Asia Mater. 2016, 8, No. e304.

(56). Reekmans K; De Vocht N; Praet J; Fransen E; Le Blon D; Hoornaert C; Daans J; Goossens H; Van der Linden A; Berneman Z; Ponsaerts P Spatiotemporal Evolution of Early Innate Immune Responses Triggered by Neural Stem Cell Grafting. Stem Cell Res. Ther 2012, 3, 56. [PubMed: 23241452]

(57). Ghuman H; Mauney C; Donnelly J; Massensini AR; Badylak SF; Modo M Biodegradation of ECM Hydrogel Promotes Endogenous Brain Tissue Restoration in a Rat Model of Stroke. Acta Biomater. 2018, 80, 66–84. [PubMed: 30232030]

(58). Fainstein N; Ben-Hur T Brain Region-Dependent Rejection of Neural Precursor Cell Transplants. Front. Mol. Neurosci 2018, 11, 136. [PubMed: 29760649]

(59). Moshayedi P; Ng G; Kwok JCF; Yeo GSH; Bryant CE; Fawcett JW; Franze K; Guck J The Relationship Between Glial Cell Mechanosensitivity and Foreign Body Reactions in the Central Nervous System. Biomaterials 2014, 35, 3919–3925. [PubMed: 24529901]

(60). Galarza S; Crosby AJ; Pak C; Peyton SR Control of Astrocyte Quiescence and Activation in a Synthetic Brain Hydrogel. Adv. Healthcare Mater 2020, 9, No. e1901419.

(61). Porambo M; Phillips AW; Marx J; Ternes K; Arauz E; Pletnikov M; Wilson MA; Rothstein JD; Johnston MV; Fatemi A Transplanted Glial restricted Precursor Cells improve Neurobehavioral and Neuropathological Outcomes in a Mouse Model of Neonatal White Matter Injury Despite Limited Cell Survival. Glia 2015, 63, 452–465. [PubMed: 25377280]

(62). Fulmer CG; VonDran MW; Stillman AA; Huang Y; Hempstead BL; Dreyfus CF Astrocyte-Derived BDNF Supports Myelin Protein Synthesis After Cuprizone-Induced Demyelination. J. Neurosci 2014, 34, 8186–8196. [PubMed: 24920623]

(63). Shinozaki Y; Nomura M; Iwatsuki K; Moriyama Y; Gachet C; Koizumi S Microglia Trigger Astrocyte-Mediated Neuroprotection via Purinergic Gliotransmission. Sci. Rep 2014, 4, 4329. [PubMed: 24710318]

(64). Dooves S; Leferink PS; Krabbenborg S; Breeuwsma N; Bots S; Hillen AEJ; Jacobs G; van der Knaap MS; Heine VM Cell Replacement Therapy Improves Pathological Hallmarks in a Mouse Model of Leukodystrophy Vanishing White Matter. Stem Cell Rep. 2019, 12, 441–450.

(65). Chan SJ; Niu W; Hayakawa K; Hamanaka G; Wang X; Cheah PS; Guo S; Yu Z; Arai K; Selim MH; Kurisawa M; Spector M; Lo EH Promoting Neuro-Supportive Properties of Astrocytes with Epidermal Growth Factor Hydrogels. Stem Cells Transl Med. 2019, 8, 1242–1248. [PubMed: 31483567]

(66). Moshayedi P; Nih LR; Llorente IL; Berg AR; Cinkornpumin J; Lowry WE; Segura T; Carmichael ST Systematic Optimization of an Engineered Hydrogel Allows for Selective Control of Human Neural Stem Cell Survival and Differentiation After Transplantation in the Stroke Brain. Biomaterials 2016, 105, 145–155. [PubMed: 27521617]

(67). Führmann T; Anandakumaran PN; Payne SL; Pakulska MM; Varga BV; Nagy A; Tator C; Shoichet MS Combined Delivery of Chondroitinase ABC and Human Induced Pluripotent Stem Cell-Derived Neuroepithelial Cells Promote Tissue Repair in an Animal Model of Spinal Cord Injury. Biomed. Mater 2018, 13, 024103. [PubMed: 29083317]

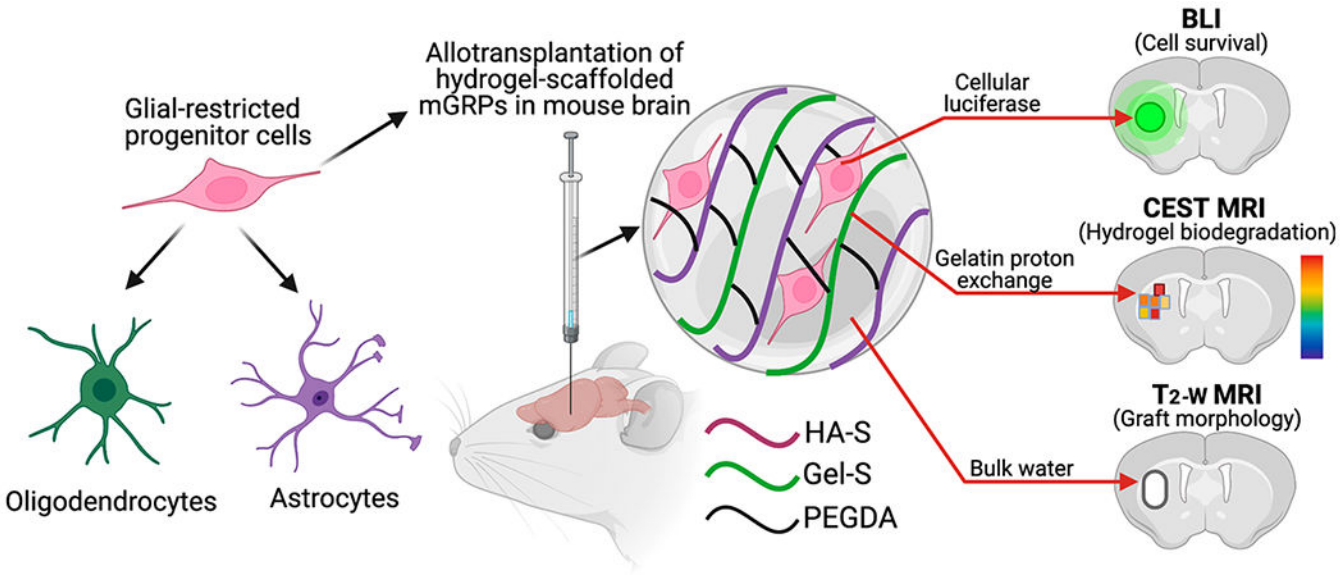

Figure 1.

Schematic outline of hydrogel-scaffolded glial progenitor transplantation and multimodal *in vivo* imaging of the graft in mouse brain.

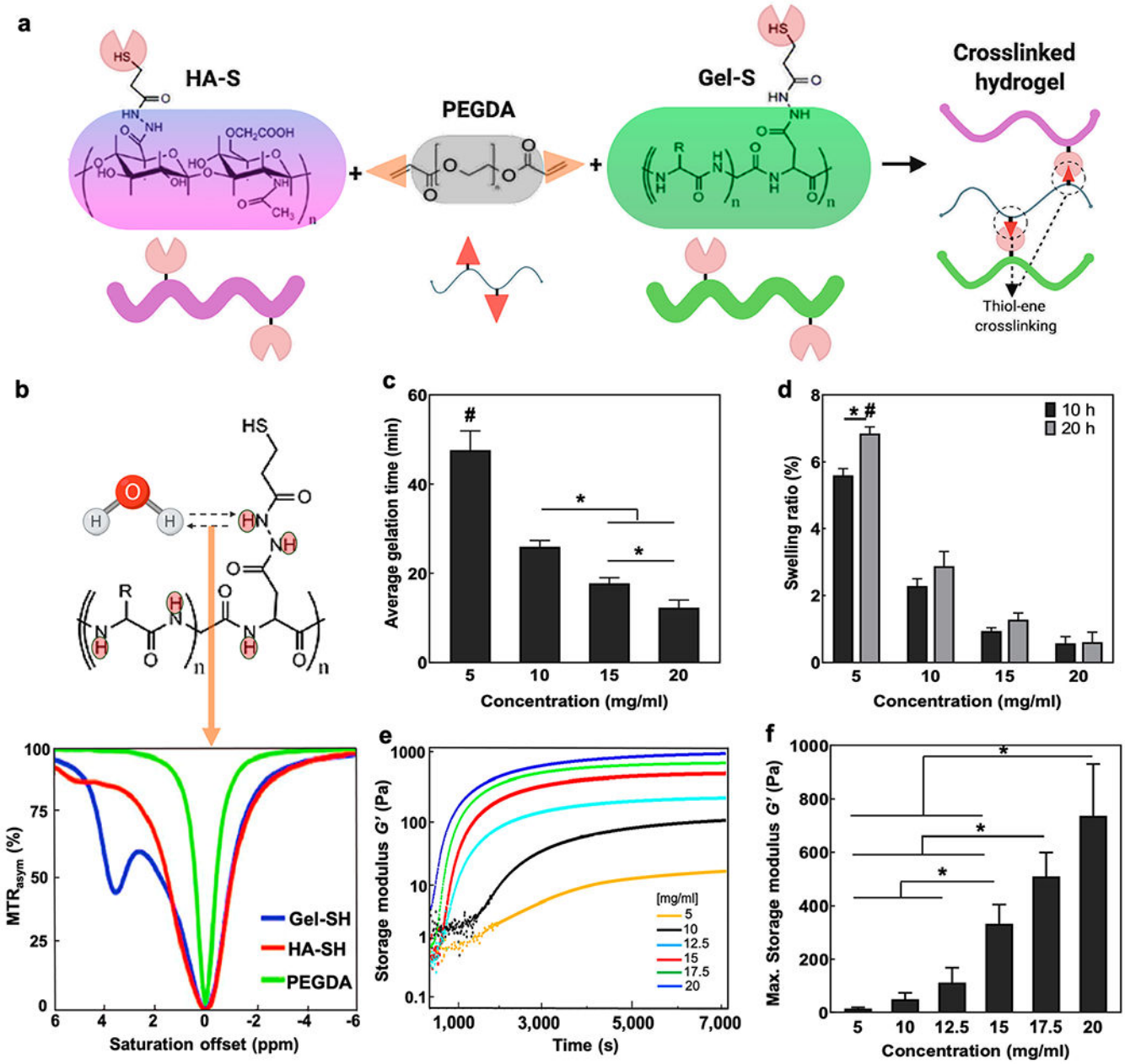

Figure 2.

Hydrogel composition, CEST properties and rheology. (a) Schematic overview of the tri-component hydrogel as prepared by HA-S and Gel-S cross-linking with PEGDA. (b) Chemical structure of Gel-S showing multiple abundant protons that are exchangeable with water protons and the Z-spectra of the three individual hydrogel components. (c) Average gelation time of composite hydrogels post cross-linking with PEGDA. (d) Percentage swelling of composite hydrogels in PBS at 10 and 20 h incubation post gelation (e) storage modulus (G') curves of the cross-linked hydrogel components over time at 37 °C. (f) Comparison of maximum storage modulus for different hydrogel formulations near

complete gelation. *$p < 0.05$ between compared groups, #$p < 0.05$ compared to all groups ($n = 5$).

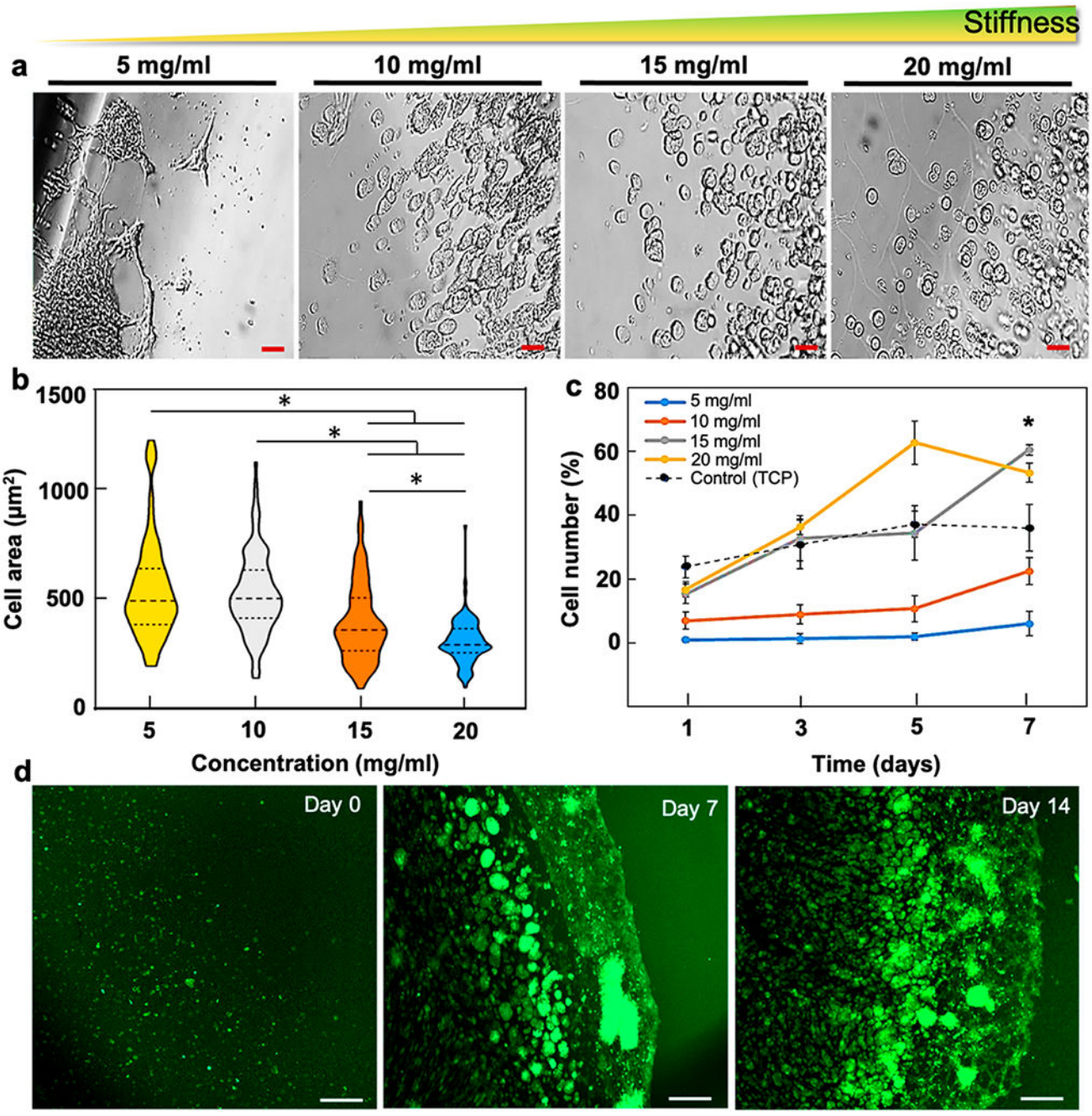

Figure 3.

mGRP morphology and viability. (a) Bright-field images of hydrogel-scaffolded mGRPs in four composite hydrogel formulations (day 4). (b) Comparison of cell spread areas for each formulation ($n = 6$ fields per formulation, 3 independent data sets, day 4). (c) Cell proliferation of hydrogel scaffolded mGRPs and control. (d) GFP^+ fluorescence images of scaffolded mGRPs in 10 mg/mL hydrogel formulation. *$p < 0.05$, ($n = 4$). Scale bar = 100 μm.

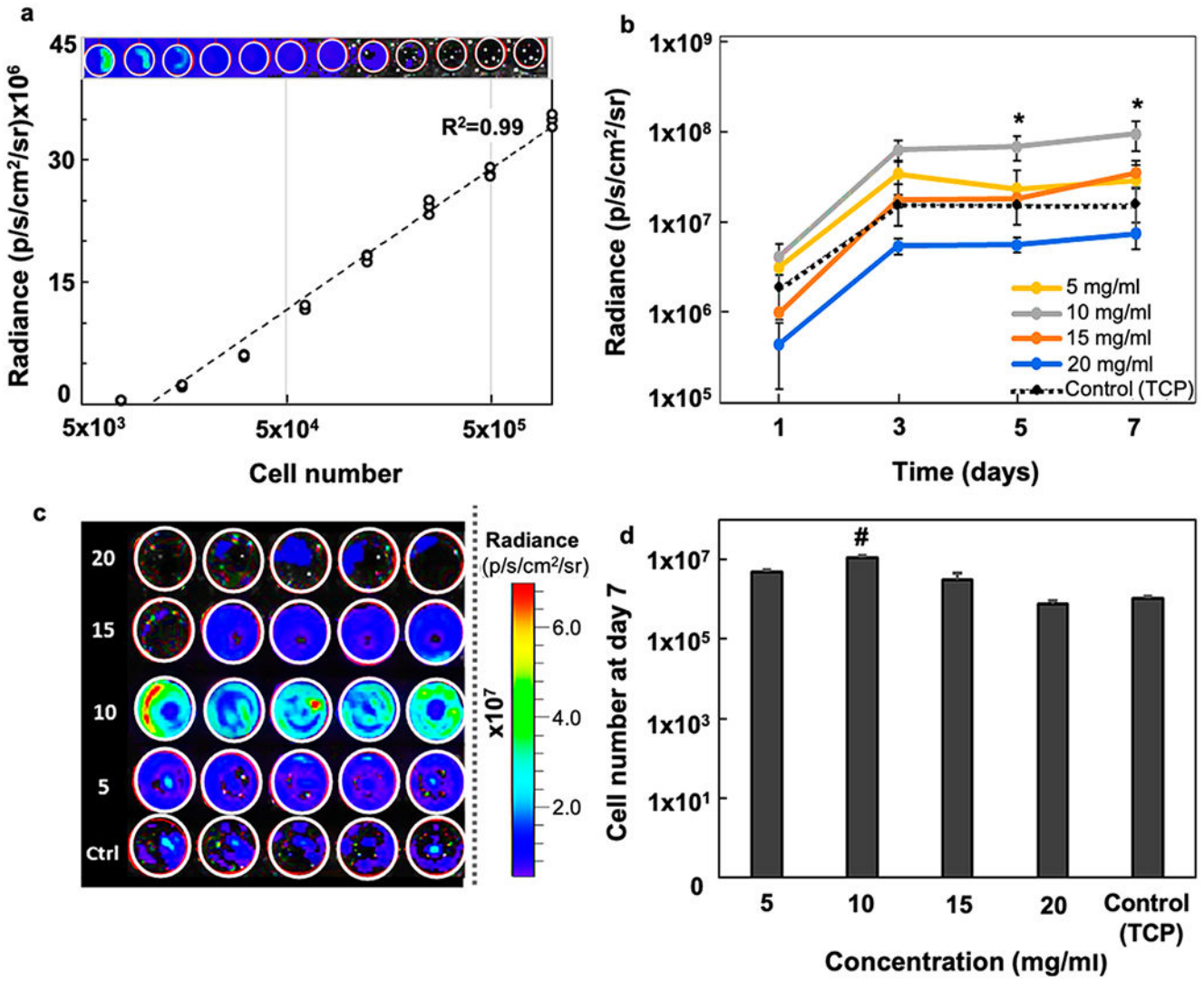

Figure 4.

In vitro BLI. (a) BLI signal intensity vs cell number for naked mGRPs in PBS (R^2 = 0.986, n = 3). (b) *In vitro* BLI signal intensity of hydrogel-scaffolded mGRPs and naked control (n = 4). (c) Representative BLI readout intensity maps at day 7. Values (left) represent different composite hydrogel densities expressed in mg/mL. (d) Comparison of corresponding cells numbers at day 7 as calculated from the BLI intensity plot shown in (a), #$p < 0.05$ as compared to all groups. *$p < 0.05$ between compared groups.

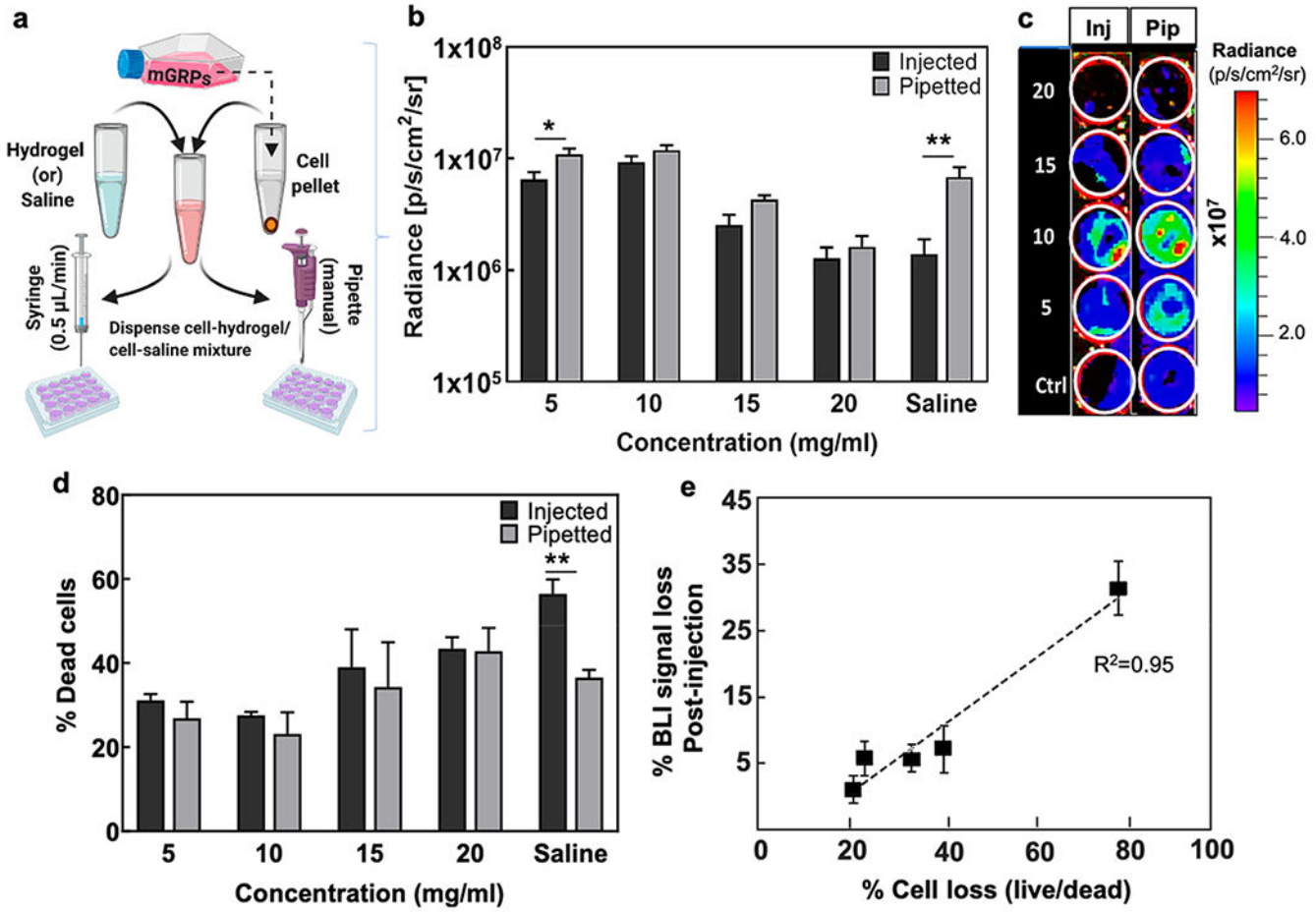

Figure 5.

Injected vs pipetted cell survival. (a) Schematic illustration of “pipetted” vs “injected” deposition of mGRPs. (b,c) BLI signal intensity and representative *in vitro* BLI image at day 1 post injection or pipetting of mGRPs ($n = 4$). Values (left) represent different composite hydrogel densities expressed in mg/mL. (d) Percentage of dead cells as determined by live/dead cell counting on 500 μm^2 areas ($n = 4$). (e) Correlation of % BLI signal loss vs % PI-positive cells ($R^2 = 0.946$). *$p < 0.05$, **$p < 0.01$ ($n = 4$).

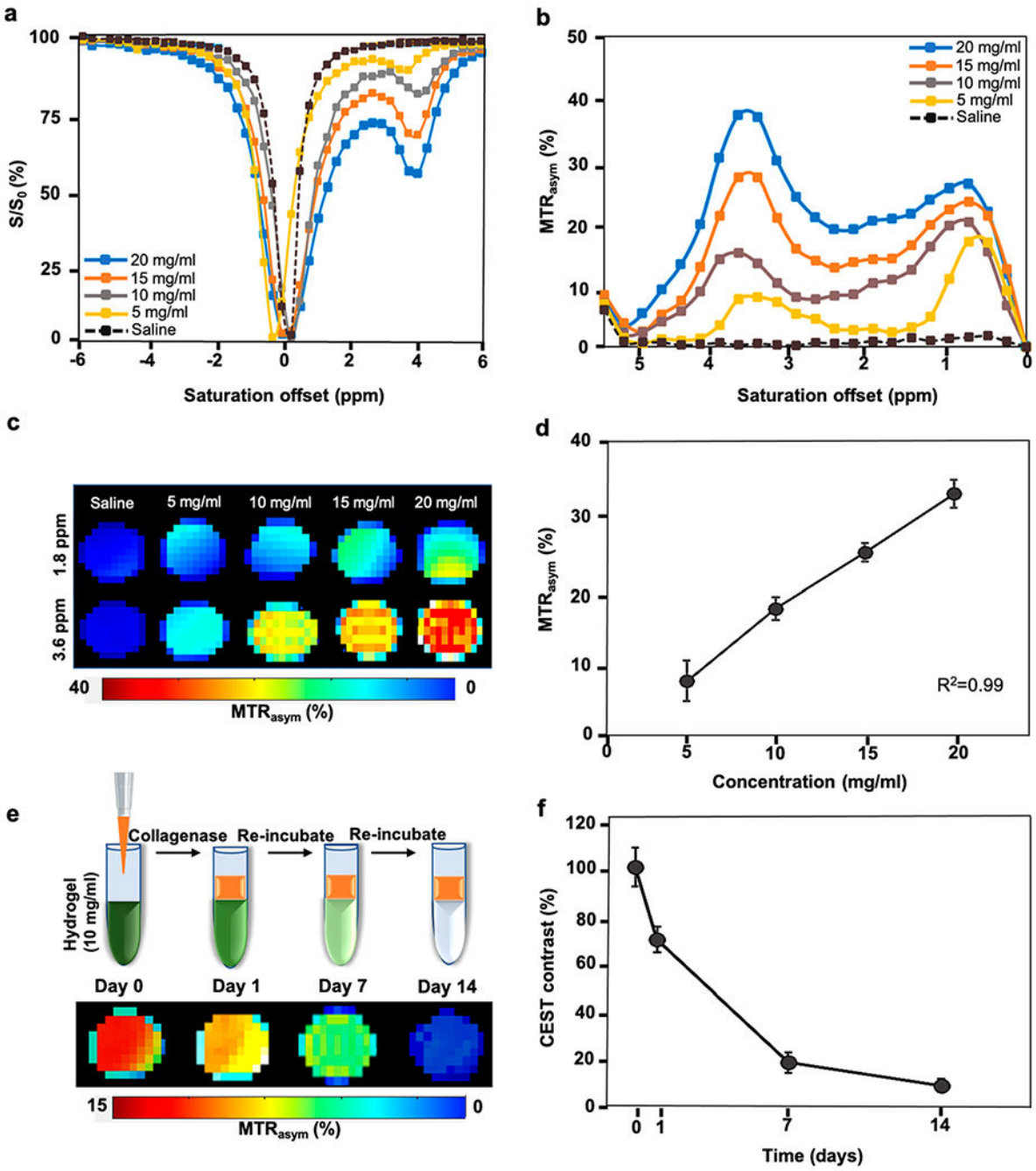

Figure 6.

CEST properties of hydrogel phantoms. (a) *In vitro* Z-spectrum. (b) *In vitro* MTR_{asym} spectra of different hydrogel formulations at a saturation power of 3.6 μT. (c) CEST maps of the hydrogels at 1.8 and 3.6 ppm offset of water. (d) MTR_{asym} values exhibiting a linear correlation with hydrogel concentration. (e) CEST maps with hydrogel degradation and (f) corresponding CEST contrast (normalized MTR_{asym} values) post enzymatic treatment of the 10 mg/mL hydrogel with collagenase.

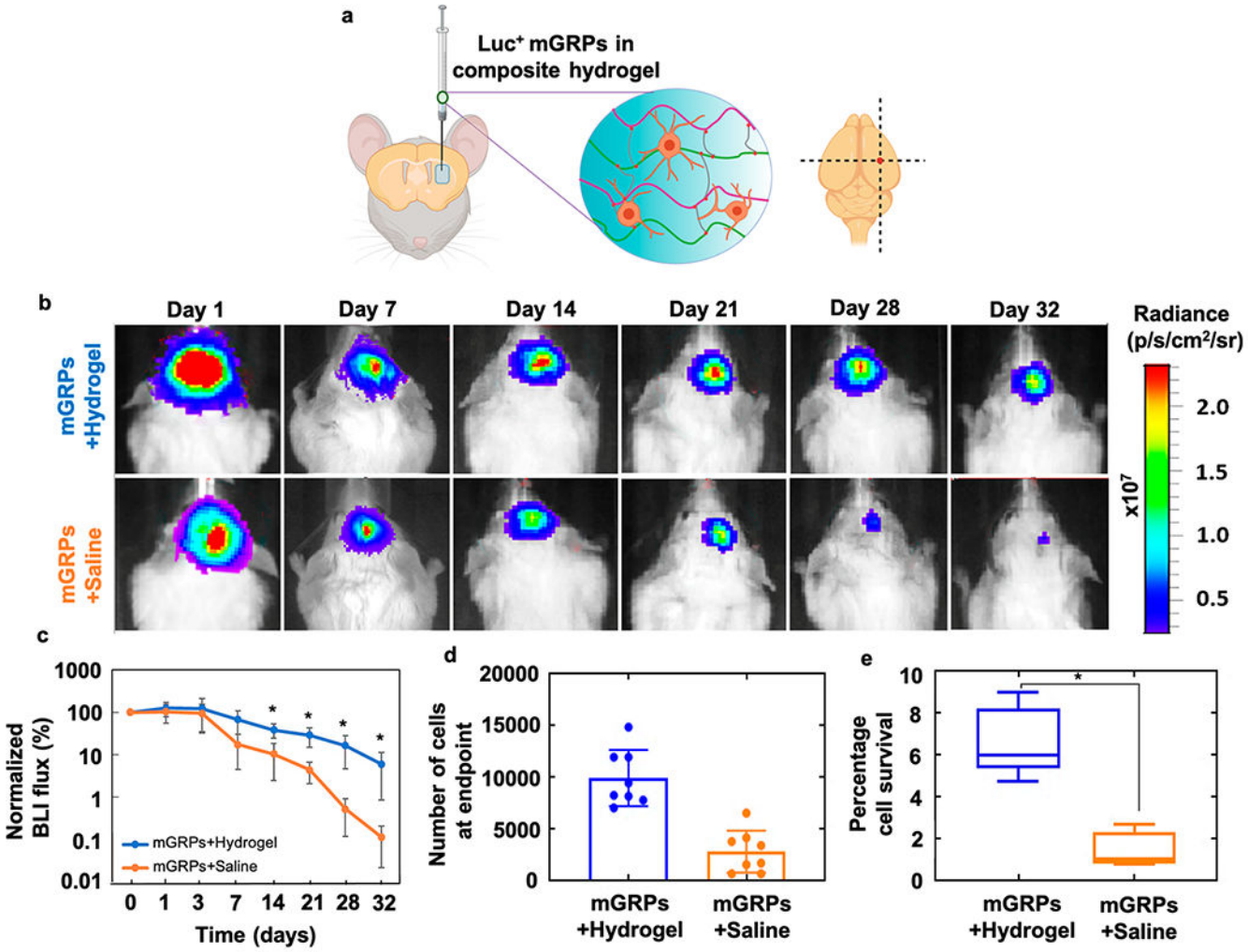

Figure 7.

Survival of intracerebral mGRP transplants: (a) scheme of transplantation of scaffolded Luc$^+$ mGRPs in mouse brain striatum. (b) Representative serial BLI images and (c) quantification of 2×10^5 mGRPs with and without scaffolding in a 10 mg/mL hydrogel transplanted in the brain striatum region of immunocompetent BALB/c mice ($n = 8$). (d) Cell numbers at the endpoint as calculated from BLI intensity readouts. (e) Percentage cells of day 0 surviving at day 32 as calculated from BLI intensity. *$p < 0.05$.

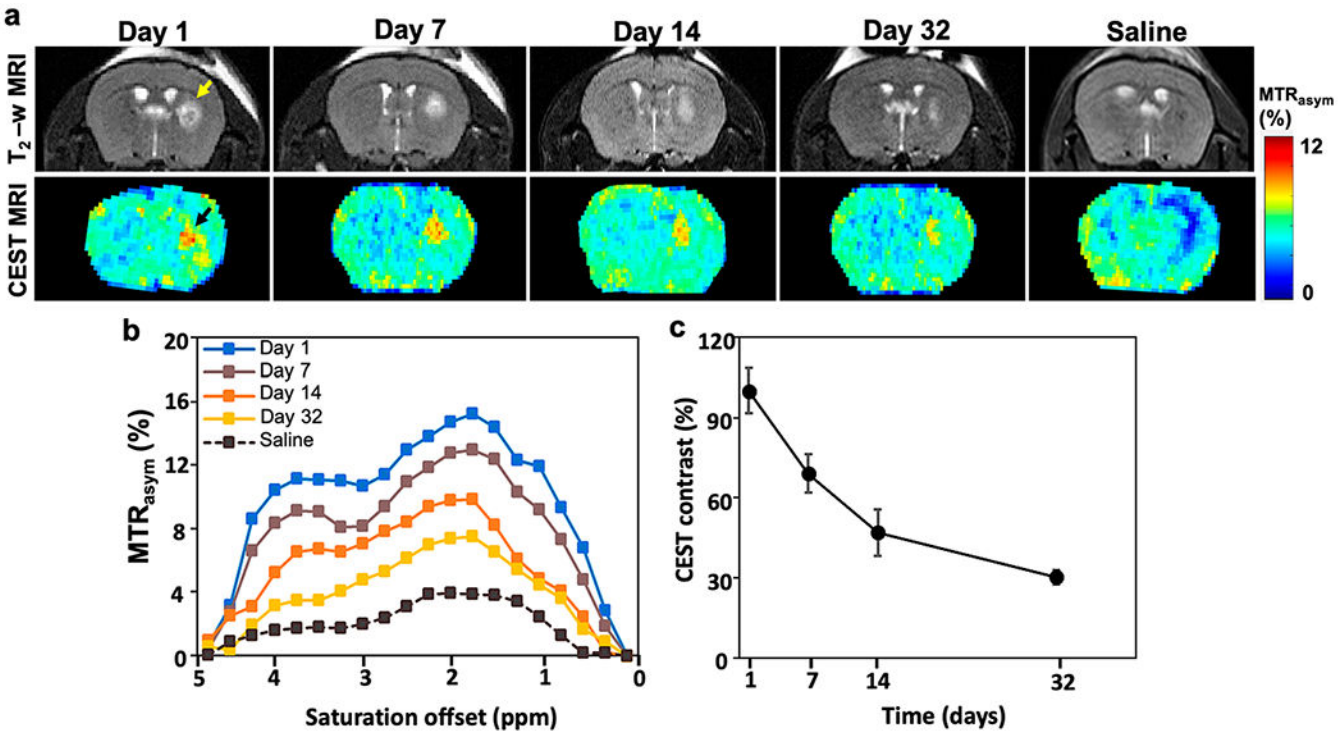

Figure 8.

In vivo T_2-*w* and CEST MRI. (a) T_2-*w* (top) and CEST MR (bottom) maps of immunocompetent BALB/c mouse brain transplanted with either scaffolded or unscaffolded (saline control) mGRPs in the right striatum. Yellow and black arrows indicate a T_2 hyperintense region and CEST contrast at the cell transplant region. (b) MTR_{asym} spectra and (c) normalized CEST contrast at 3.6 ppm on the transplant site at different time points until day 32.

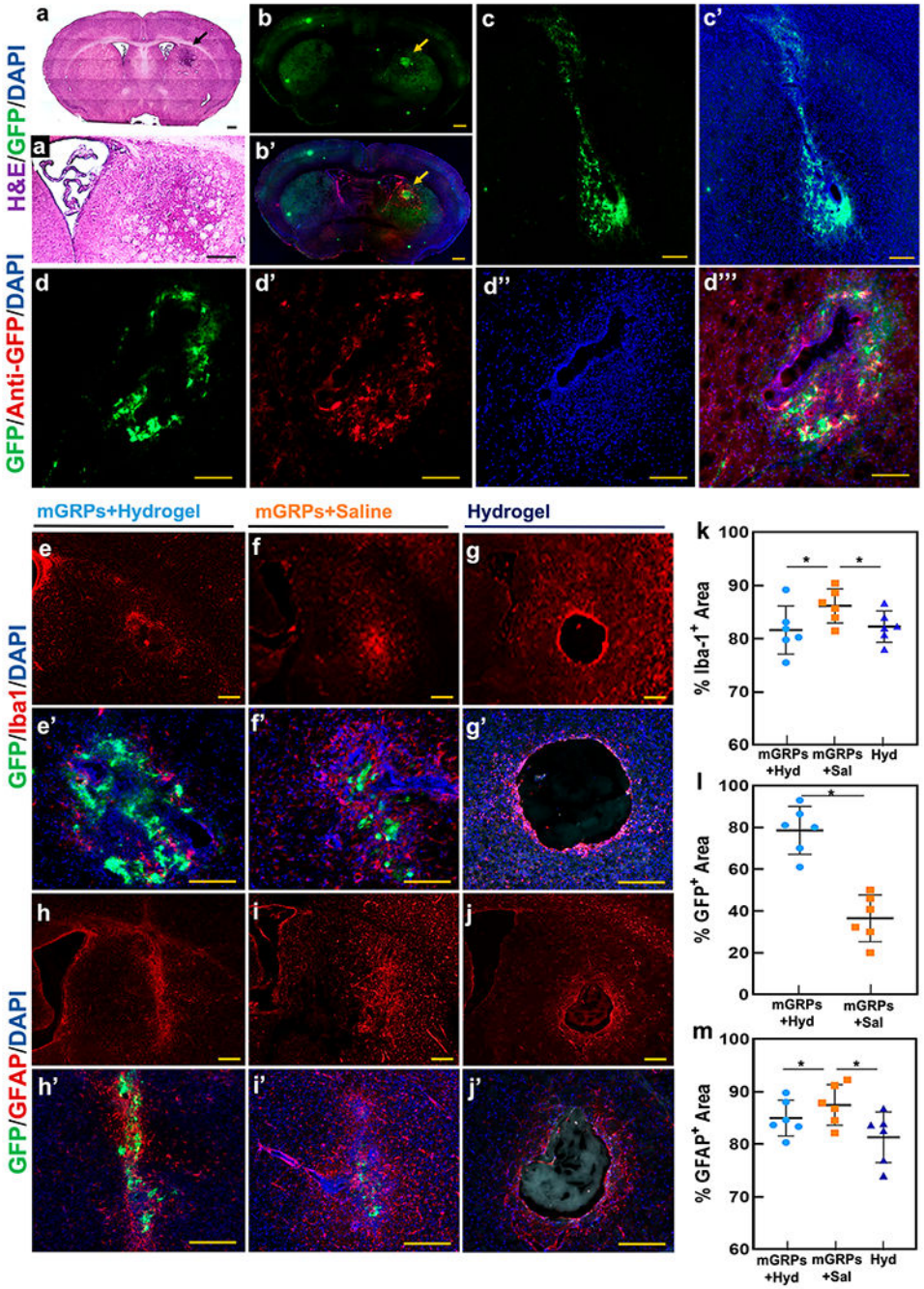

Figure 9.

Immunohistological assessment of graft fate. (a,a′) Whole brain and enlarged view of H&E-stained brain sections containing scaffolded GFP$^+$ mGRPs (black arrow) at day 14 post transplantation. (b,b′) Whole brain section containing the GFP$^+$ mGRP + hydrogel transplantation site and overlay of the graft region with anti-Iba-1 and DAPI staining. (c,c′) High magnification view of graft region with GFP$^+$ mGRPs and DAPI overlay. (d–d‴) Anti-GFP and DAPI overlay of GFP$^+$ mGRP graft site. (e–g) Anti-Iba-1 and (h–j) anti-GFAP immunostaining of the graft regions at day 14 for hydrogel-scaffolded mGRPs,

naked cells, and hydrogel only. (e′–g′) and (h′–j′) High magnification images of the GFP^+ region overlaid on Iba-1^+ and $GFAP^+$ regions. (k–m) Quantitative comparison of Iba-1^+, $GFAP^+$, and GFP^+ regions for hydrogel-scaffolded mGRPs, naked cells, and hydrogel only. *$p < 0.05$, $n = 4$. Scale bar = 100 μm.

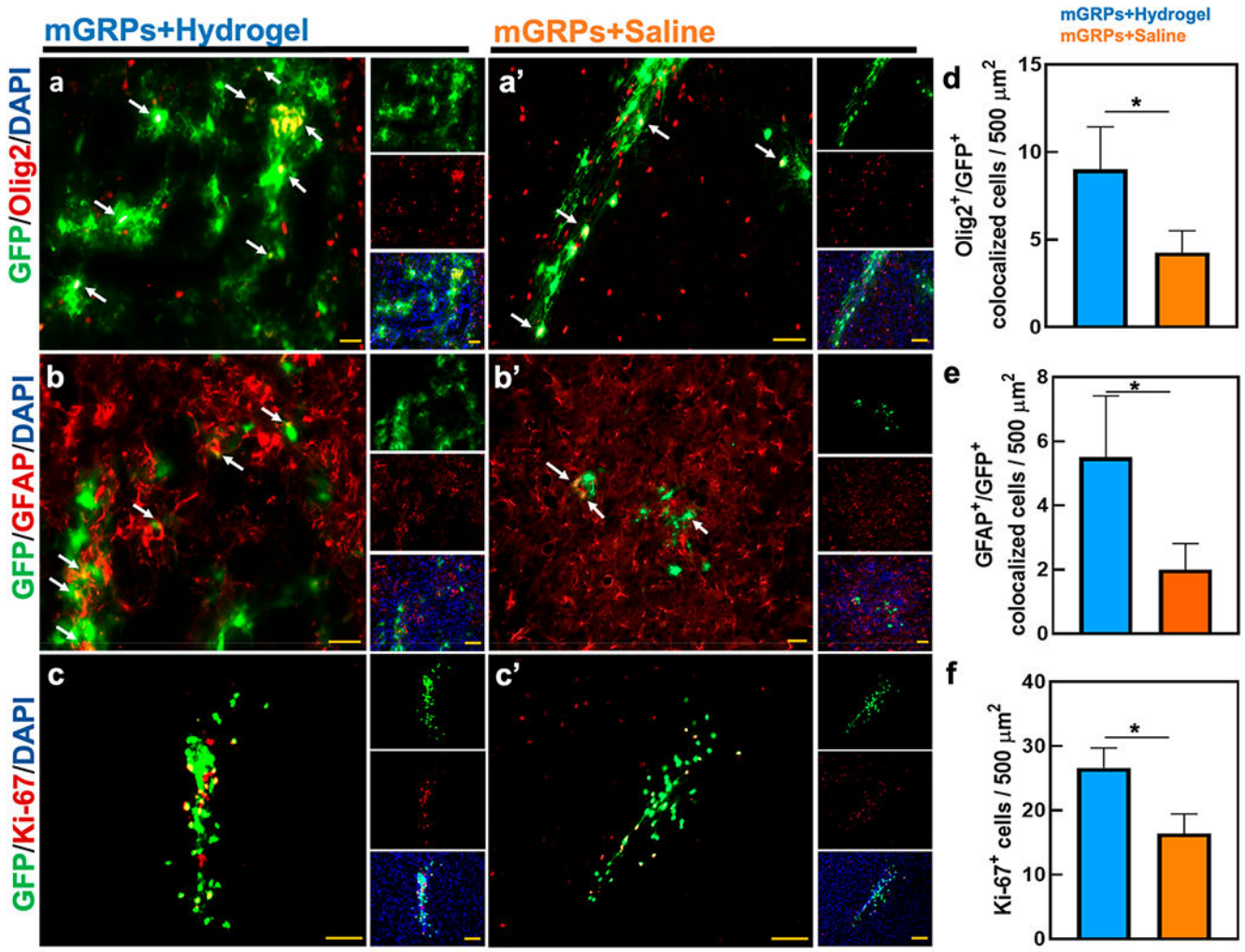

Figure 10.

Differentiation of mGRPs. Expression of (a,a′) Olig2, (b,b′) GFAP, and (c,c′) Ki-67 in mGRPs engrafted with a 10 mg/mL hydrogel or saline at 4 weeks post-striatal transplantation. Shown are the merged marker/GFP$^+$ images with separate staining and DAPI nuclear staining in insets. (d–f) Quantitative comparison of Olig2/GFAP/Ki-67 expression/co-localization between scaffolded and naked mGRP grafts. *$p < 0.05$, $n = 5$. Scale bar = 50 μm.